

Density Estimation via Measure Transport: Outlook for Applications in the Biological Sciences

Vanessa López-Marrero^{*,†,‡} Patrick R. Johnstone[§] Gilchan Park[†] Xihaier Luo[†]

January 2, 2024

Abstract

One among several advantages of measure transport methods is that they allow for a unified framework for processing and analysis of data distributed according to a wide class of probability measures. Within this context, we present results from computational studies aimed at assessing the potential of measure transport techniques, specifically, the use of triangular transport maps, as part of a workflow intended to support research in the biological sciences. Scarce data scenarios, which are common in domains such as radiation biology, are of particular interest. We find that when data is scarce, sparse transport maps are advantageous. In particular, statistics gathered from computing series of (sparse) adaptive transport maps, trained on a series of randomly chosen subsets of the set of available data samples, leads to uncovering information hidden in the data. As a result, in the radiation biology application considered here, this approach provides a tool for generating hypotheses about gene relationships and their dynamics under radiation exposure.

1 Introduction

The problem of estimating a probability distribution density from samples (e.g., observations, measurements, or simulation data) is ubiquitous in data science, uncertainty quantification, clustering and classification, and probabilistic modeling and inference tasks. Moreover, it is common among various scientific and engineering fields, including biology [38, 14, 1, 41, 5, 7, 12, 39]. Often, well-known parametric density functions (dependent on few parameters), such as the Gaussian or Weibull density distribution functions, are adopted. While this may simplify certain tasks (e.g., computational ones), many of these known density distribution functions are not necessarily suitable for characterizing data that exhibit complex features, such as (spatial and/or temporal) correlations and non-Gaussian characteristics. For instance, as reported in [7], accounting for differences in the distribution densities of gene expressions can lead to improved interpretation of cancer transcriptomic data. Hence, a density estimation framework capable of characterizing a diverse range of properties is highly desirable. A measure transport approach [44, 37, 36] offers this possibility.

Optimal measure transport, broadly defined, deals with the problem of minimizing the cost of transporting one (probability) measure to another. The subject has a long history with significant

*Corresponding author. E-mail: vlopezmar@bnl.gov

†Computational Science Initiative, Brookhaven National Laboratory

‡Institute for Advanced Computational Science (IACS), Stony Brook University.

§Work performed while at the Computational Science Initiative, Brookhaven National Laboratory. Current affiliation: Meta.

impact in many fields of mathematics, such as probability theory, optimization, and partial differential equations, among others [44, 37]. Current interest on the topic stems from its potential in numerous areas, including density estimation, data science, machine learning, Bayesian inference, sampling, and data assimilation [1, 42, 41, 24, 8, 40, 36, 32, 11, 39, 45, 17]. Among various measure transport techniques under active research, we mention the use of triangular transport maps, normalizing/gradient flows, diffusion maps, and invertible neural networks. Although differing in the particulars, affording a unified framework for processing and analysis of data from a range of distributions (Gaussian, non-Gaussian, uni-modal, multi-modal, etc.) is a powerful property common to all.

In this paper we consider measure transport for density estimation from data, in particular the use of triangular transport maps, envisioning its potential within a computational workflow for tasks associated with biological applications. The motivating problem, which is density estimation (or prior/posterior construction) when data is scarce, as well as the proposed workflow, are described in Section 2. Overviews of the topics of measure transport and density estimation via triangular transport maps appear, respectively, in Sections 3 and 4. References for thorough treatments of these subjects are provided therein. Computational experiments performed using gene expression data are presented in Section 5.

2 Motivating Application

The present work stems from the conception of a comprehensive computational workflow intended to support research in the biological sciences, in particular the radiation biology domain. Within this effort, our interest is in enabling a *unified* framework where probabilistic modeling, inference, and statistical analyses can be carried out for a wide range of data distributions. As noted in the Introduction (Section 1), measure transport offers the possibility of such unified approach. We envision measure transport techniques comprising one component within the larger scope, as depicted in Figure 1.

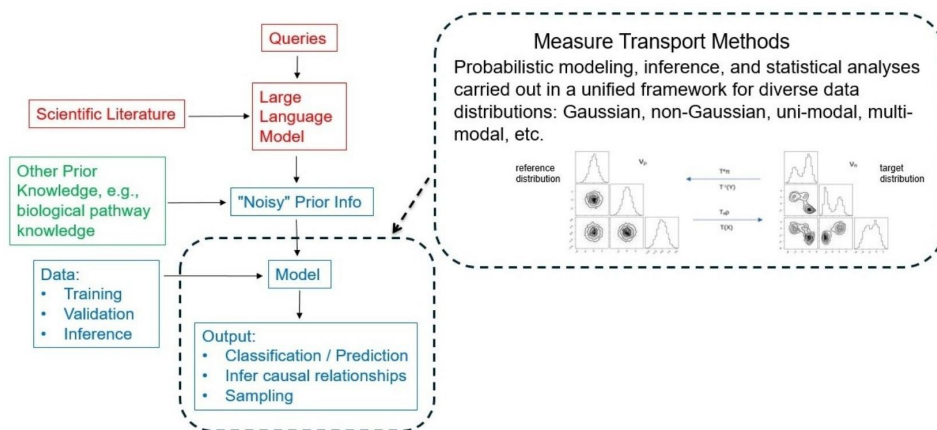


Figure 1: Computational workflow for probabilistic modeling, inference, and statistical analyses. To account for scarcity of data, model training can be augmented with prior knowledge. Such prior knowledge may come from large language models or human experts, for instance. Measure transport techniques allow for a unified framework for dealing with data exhibiting diverse characteristics.

One motivating problem within the framework from Figure 1 is that of probability distribution density estimation for phenotypic classification problems, for example, for inferring class labels,

such as radiation exposure levels or cancer types, given sample data. Normalizing flows (one kind among the various measure transport methods) have been successfully used for clustering and classification in the cancer domain [1]. Now, when data is scarce, regardless of the density estimation technique adopted, prior knowledge (associated with the particular application) may be used in conjunction with data to estimate the class-conditional densities. In the work [5], the authors proposed incorporation of prior knowledge from biological pathways for class-conditional density estimation as one approach for optimal Bayesian classifier design when data availability is limited. Here we also consider the use of prior knowledge from biological pathways, along with measure transport techniques, in the computational experiments reported in Section 5. In the workflow from Figure 1, we envision prior knowledge coming from other sources as well, such as large language models [33, 34] and human experts. This is the subject of future work.

The reader is referred to [14] for a thorough treatment of the topic of classification via probability density distribution functions (kernel density classification, per the terminology from [14]), among many other classification methods. We summarize next what is needed to make the discussions in Sections 4.2 and 5 (appearing later in the manuscript) self-contained. Assume we have K classes to infer sample membership from. Upon computing, separately, an estimated probability density distribution function π_k for each class k , where $k = 0, \dots, K - 1$, the probability $\Pr(C = k | \mathcal{Y} = y)$ that a given sample y belongs to class k can be obtained from the class-conditional densities $\{\pi_l\}_{l=0}^{K-1}$ via

$$\Pr(C = k | \mathcal{Y} = y) = \frac{\hat{\pi}_k \pi_k(y)}{\sum_{l=0}^{K-1} \hat{\pi}_l \pi_l(y)}, \quad (1)$$

where $\{\hat{\pi}_l\}_{l=0}^{K-1}$, $\sum_{l=0}^{K-1} \hat{\pi}_l = 1$, are estimates for the class prior probabilities. The latter may be determined from the proportion of training samples, for instance, or other prior knowledge.

Finally, in Section 5.2 we discuss how, as part of the computational framework from Figure 1, measure transport methods have the potential to address other problems, in addition to the above-mentioned classification one. More precisely, by uncovering information hidden in the data, adaptive transport maps [2] could provide a means for generating hypotheses regarding gene relationships for the radiation biology application considered in Section 5.2. Before getting into such details, we now continue with an overview of required topics from measure transport theory.

3 Basics of Measure Transport

As mentioned in the Introduction (Section 1), optimal measure transport addresses the problem of minimizing the cost of transporting one (probability) measure to another. We now give a summary of the basic concepts, as they relate to the problem of density estimation which is of interest to us. For a thorough treatment of the subject of measure transport, the reader may refer to [44, 37, 19, 4] (theory), [24, 36, 2] (computational), and references therein.

Informally, given two probability measures ν_ρ and ν_π defined on the algebra of Borel sets of \mathbb{R}^m , $m \geq 1$, and absolutely continuous with respect to the Lebesgue measure dx on \mathbb{R}^m , with densities ρ and π , respectively, an invertible map $T: \mathbb{R}^m \rightarrow \mathbb{R}^m$ transports ν_ρ to ν_π if and only if

$$\nu_\pi(B) = \nu_\rho(T^{-1}(B)) \quad (2)$$

for every Borel set $B \subset \mathbb{R}^m$. One says the map T pushes forward ν_ρ to ν_π , denoted $T_{\#}\nu_\rho = \nu_\pi$. Since we assume that both probability measures ν_ρ and ν_π are absolutely continuous with respect to the Lebesgue (volume) measure dx on \mathbb{R}^m , one may identify them with their probability densities

ρ and π . That is, $\nu_\rho(dx) = \rho dx$ and $\nu_\pi(dx) = \pi dx$. Moreover, we restrict the class of maps T that we consider to the class of differentiable or even infinitely differentiable invertible maps. With these assumptions one can write the measure transport equation (2) in terms of densities. Namely, the density ρ is the *pullback* $T^\# \pi$ of the density π ,

$$\rho(\cdot) = T^\# \pi(\cdot) = \pi(T(\cdot)) |\det J_T(\cdot)|, \quad (3)$$

where J_T is the Jacobian matrix of T . Conversely, the inverse T^{-1} of T pushes forward ν_π to ν_ρ , denoted $(T^{-1})_\# \nu_\pi = \nu_\rho$, and π is the pullback $(T^{-1})^\# \rho$ of ρ :

$$\pi(\cdot) = (T^{-1})^\# \rho(\cdot) = \rho(T^{-1}(\cdot)) |\det J_{T^{-1}}(\cdot)|, \quad (4)$$

where $J_{T^{-1}}$ is the Jacobian matrix of T^{-1} . An illustration of these fundamental concepts appears in Figure 2.

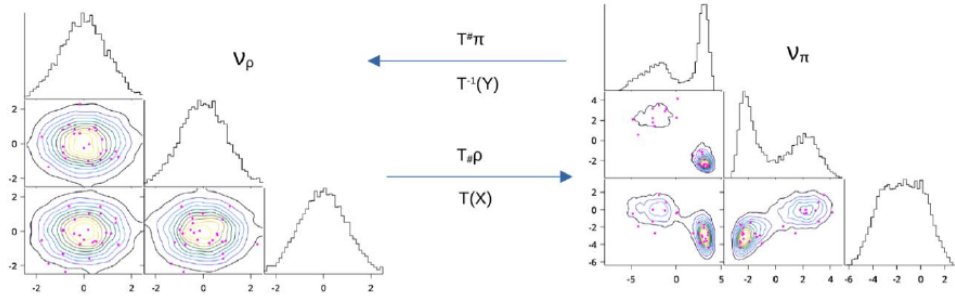


Figure 2: The map $T : \mathbb{R}^3 \rightarrow \mathbb{R}^3$ transports samples from ν_ρ , a multivariate standard normal (i.e., Gaussian), to samples from ν_π , a multivariate, multi-modal density distribution. The density ρ is the pullback $T^\# \pi$ of the density π . Conversely, the map T^{-1} transports samples from ν_π to samples from ν_ρ . The density π is the pullback $(T^{-1})^\# \rho \equiv T^\# \rho$ of the density ρ . Contour plots of the corresponding one- and two-dimensional marginal distribution densities also are shown.

Recall that we are concerned with the problem of estimating an unknown probability density function characterizing some given data set of samples or observations, for instance, gene expression data. Denote the corresponding unknown probability measure by ν_π and call it the *target* measure. On the other hand, let ν_ρ be a probability measure amenable to computations, for example, the standard normal $\mathcal{N}(0, I)$, so one can easily draw samples from it and evaluate its density ρ . Call this the *reference* measure. Now, let $\mathcal{X} = (\mathcal{X}_1, \mathcal{X}_2, \dots, \mathcal{X}_m)$ and $\mathcal{Y} = (\mathcal{Y}_1, \mathcal{Y}_2, \dots, \mathcal{Y}_m)$ be random vectors with probability distribution functions $F_{\mathcal{X}}$ and $F_{\mathcal{Y}}$, respectively, such that $dF_{\mathcal{X}} = \nu_\rho$ and $dF_{\mathcal{Y}} = \nu_\pi$. The random vectors \mathcal{X} , \mathcal{Y} assume, respectively, values $x, y \in \mathbb{R}^m$ (also denoted by $x \sim \nu_\rho$ and $y \sim \nu_\pi$). Then if $X = \{x \in \mathbb{R}^m : x \sim \nu_\rho\}$ and $Y = \{y \in \mathbb{R}^m : y \sim \nu_\pi\}$ are sets of samples formed from the values of the random vectors \mathcal{X} and \mathcal{Y} (i.e., the elements in X are distributed according to ν_ρ , and those in Y are distributed according to ν_π) the transport map should satisfy $\nu_\pi(Y) = \nu_\rho(T^{-1}(Y))$.

Thus, given the sets of samples X and Y , our goal is to *learn* (or compute) the transport map T and use it later as a predictor for the values of \mathcal{Y} (and therefore an estimator of ν_π). The set Y consists of samples (usually taken from experiment) of the random vector \mathcal{Y} distributed according to an *a priori unknown* target probability measure ν_π , while the reference probability measure ν_ρ is *a priori known* (e.g., Gaussian) and the set X is generated from samples of a random vector \mathcal{X} distributed according to ν_ρ . Under the assumption that one can compute such a map T transporting between the target and reference measures, the framework outlined herein and depicted in Figure

2 yields a method for approximating the desired unknown density function that characterizes the given sample data set. Then, the central problem is to compute, or learn, such a map T . This problem is further addressed in Section 4.

Upon learning such a map T from data, evaluation of the (unknown) density π at a given (new) sample $y \sim \nu_\pi$ can be done via equation (4) as, by construction, all the functions on the right-hand side of equation (4) are known and can be evaluated. Moreover, because the reference measure is chosen to make sampling from it an easy and efficient task, sampling from the target measure can be done efficiently by drawing samples from the reference and transporting them to the target via the learned map T . Thus, probabilistic modeling, inference, and statistical analyses in the target space are enabled by such measure transport framework.

4 Transport Map Computation

To compute transport maps, we use software [28, 3] made available by the MIT Uncertainty Quantification (MUQ) Group [27]. The reader is referred to the original publications [10, 24, 40, 2] for complete descriptions of the numerical methods and software libraries. A summary is provided next, to make the present manuscript self-contained.

Let ν_ρ and ν_π be two (probability) measures defined on the algebra of Borel sets of \mathbb{R}^m , $m \geq 1$. Suppose that $T : \mathbb{R}^m \rightarrow \mathbb{R}^m$ is a transport map pushing forward ν_ρ to ν_π . That is, it satisfies the equation

$$\nu_\pi = T_{\#}\nu_\rho \tag{5}$$

for T . By definition (see Section 3),

$$\nu_\rho = (T^{-1})_{\#}\nu_\pi \tag{6}$$

also holds. The transport map T has m components

$$T_i(x_1, x_2, \dots, x_m), \quad i = 1, \dots, m, \tag{7}$$

and one has that $y_i = T_i(x_1, x_2, \dots, x_m)$, where $y = (y_1, y_2, \dots, y_m) \sim \nu_\pi$ and $x = (x_1, x_2, \dots, x_m) \sim \nu_\rho$. Conversely, the inverse transport map T^{-1} of T has m components

$$(T^{-1})_i(y_1, y_2, \dots, y_m), \quad i = 1, \dots, m, \tag{8}$$

and one has that $x_i = (T^{-1})_i(y_1, y_2, \dots, y_m)$.

A transport map T is computed via the solution of equation (5) and a minimization problem with cost or objective function $C_\rho(T)$ generally defined as

$$C_\rho(T) = \int_{\mathbb{R}^m} c(x, T(x)) \nu_\rho(dx). \tag{9}$$

The structure of the map T depends on ρ , π , and $c(\cdot, \cdot)$. Many types of maps (not necessarily optimal), or couplings, exist between measures [44, 36]. In this study we consider the use of triangular transport maps, as they enable practical numerical computation of a transport map and its inverse [24, 2].

4.1 Triangular Transport Maps

A transport map $T : \mathbb{R}^m \rightarrow \mathbb{R}^m$, $\nu_\pi = T_{\#}\nu_\rho$, is *triangular* if

$$y_i = T_i(x_1, x_2, \dots, x_i), \quad i = 1, \dots, m. \quad (10)$$

In other words, the i -th component T_i of a triangular transport map T only depends on the values $\{x_j\}_{j=1}^i$ of the first i random variables $\{\mathcal{X}_j\}_{j=1}^i$. Thus, the map components are

$$T(x) = \begin{bmatrix} T_1(x_1) \\ T_2(x_1, x_2) \\ T_3(x_1, x_2, x_3) \\ \vdots \\ T_m(x_1, x_2, \dots, x_m) \end{bmatrix}. \quad (11)$$

Conversely,

$$x_i = (T^{-1})_i(y_1, y_2, \dots, y_i), \quad i = 1, \dots, m. \quad (12)$$

To ensure positivity of the densities (3) and (4), each map component T_i in equation (10) must be differentiable with respect to x_i , and it must hold that $\partial_{x_i} T_i > 0$, for every $i = 1, \dots, m$. We refer to the latter as the class of increasing triangular maps. Similarly, each component $(T^{-1})_i$ (12) of the inverse map T^{-1} of T must satisfy said properties with respect to the variables y_i [4, 24]. Furthermore, when both ν_ρ and ν_π are absolutely continuous with respect to the Lebesgue measure dx on \mathbb{R}^m with densities ρ and π , respectively, if $c(x, T(x)) = \|x - T(x)\|^2$, where $\|\cdot\|$ is the Euclidean distance on \mathbb{R}^m , and ν_ρ is Gaussian, instead of (9) one may seek to minimize the relative entropy, or Kullback-Leibler divergence,

$$\mathrm{D}_{\mathrm{KL}}(\nu_\pi \parallel \nu_\rho) = \int_{\mathbb{R}^m} \pi \log(\pi/\rho) dx = \mathbb{E}_\pi(\log(\pi/\rho)), \quad (13)$$

as $C_\rho(T) \leq 2A \mathrm{D}_{\mathrm{KL}}(T_{\#}\nu_\rho \parallel \nu_\rho)$, where $A > 0$ is a constant [31, 19, 4]. Under the assumption that the map T is differentiable or even smooth (*cf.* formula (28) in Appendix A), one may also look at the problem of computing an optimal transport map T as a solution of the optimization problem $\arg \min_T C_\rho(T)$, or indeed

$$\arg \min_T \mathrm{D}_{\mathrm{KL}}(T_{\#}\nu_\rho \parallel \nu_\rho), \quad (14)$$

(conversely, $\arg \min_T \mathrm{D}_{\mathrm{KL}}(\nu_\pi \parallel (T^{-1})_{\#}\nu_\pi$) under the partial differential equation constraint (3) for the map T (conversely, constraint (4) for the map T^{-1}).

Triangular maps enable efficient numerical computation of a transport map and its inverse, which is also triangular. Moreover, triangular transport maps are well-suited for conditional density estimation and sampling [10, 24, 40, 2, 17]. Techniques for computational efficiency and scalability to high-dimensional problems include, among others, composition of low order maps [10] and the use of *sparse triangular transport maps* [29, 40, 2, 17]. For such sparse maps, any given map component $(T^{-1})_i$ in equation (12) may depend only on a proper subset (possibly empty) of the variables $\{y_j\}_{j=1}^{i-1}$ and on y_i . Dependence on y_i is required. A *diagonal map*, in particular, has $x_i = (T^{-1})_i(y_i)$ for each $i = 1, \dots, m$. The random variables that a given map component depends on is referred to as the set of active variables for the map component. Collectively, they define a sparsity pattern for the transport map. For a summary of these notions, see Figure 3.

Sparse triangular transport maps can be computed without a sparsity pattern specified a priori, using specially designed algorithms which have been shown to perform well for density estimation

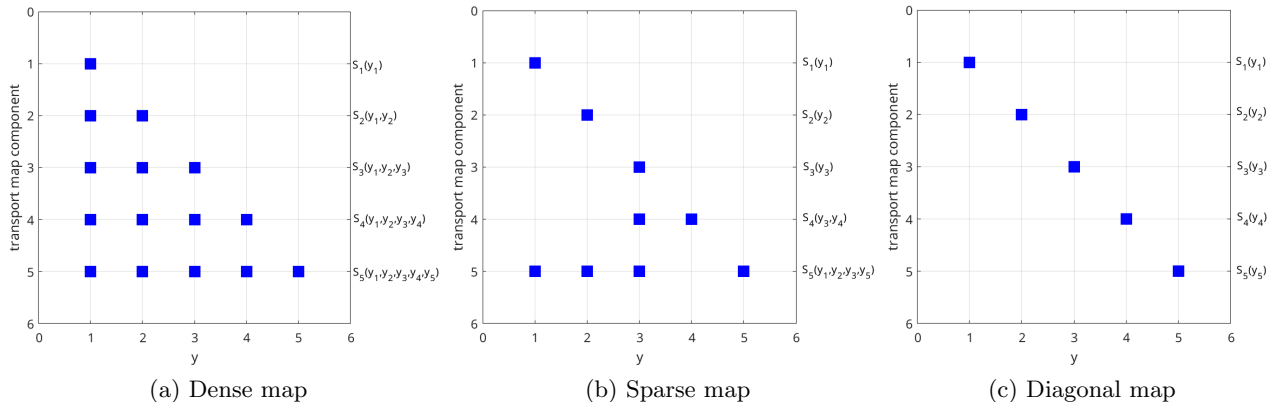


Figure 3: Pictorial representation of triangular transports maps. To simplify notation in Subfigures 3a–3c, we denote $S \equiv T^{-1}$ for the transport map T^{-1} from (12). In this example, $S : \mathbb{R}^5 \rightarrow \mathbb{R}^5$. In each plot, the horizontal axis indexes the random variables $\{\mathcal{Y}_j\}_{j=1}^5$ and the vertical axis indexes the map components $\{S_i\}_{i=1}^5$. A square appears at the intersection of grid point (j, i) if the i -th map component S_i depends on the value y_j of the j -th random variable \mathcal{Y}_j . For any given map component, the set of *active variables* is the set of random variables that the map component depends on. Collectively, the active variables define a sparsity pattern for the transport map.

problems even when sample data is limited in amount [2]. Alternatively, a desired sparsity pattern could be specified explicitly and enforced when computing a transport map. As discussed in Section 2, one motivation for our research is density estimation from samples when available data is scarce. We hence consider sparse maps for our motivating application, as expanded upon in Section 5 further below. Next, we conclude the current Section 4 with some brief comments on density estimation via triangular transport maps and several illustrative examples.

4.2 Density Estimation from Data

Referring to equations (5)–(6), recall from Section 3 that we designate the probability measure ν_ρ as the reference measure and the probability measure ν_π as the target measure. The target density π is unknown, but samples from the target measure ν_π are available. On the other hand, the reference measure ν_ρ is chosen to be known and so that it is amenable to computations and sampling. The reference measure is often selected to be the standard normal $\mathcal{N}(0, I)$, and that is our choice in all of our experiments.

Given a set of samples from the target measure ν_π , we use software libraries [28, 3] made available by the MIT Uncertainty Quantification (MUQ) Group [27] to compute a transport map (and its inverse) between the unknown target and reference measures. The transport map is computed as the solution of an optimization problem with objective function (13), using the Sample Average Approximation (SAA) algorithm. The reader is referred to [24] for full details.

Upon computation of the transport map, the target density π can be evaluated via equation (4). Given a (new) sample $y \sim \nu_\pi$, the value $\pi(y)$ can thus be obtained and used as needed, for instance for the classification problem from our motivating application, which was described in Section 2. The MUQ software libraries [28, 3] provide functionality for evaluating the target density, among many other capabilities.

To describe an application of the measure transport framework, in Figure 4 are displayed computed approximations to density functions for univariate measures. The triangular transport maps for these approximations were computed using the TransportMaps library [28], version 2.0b3.

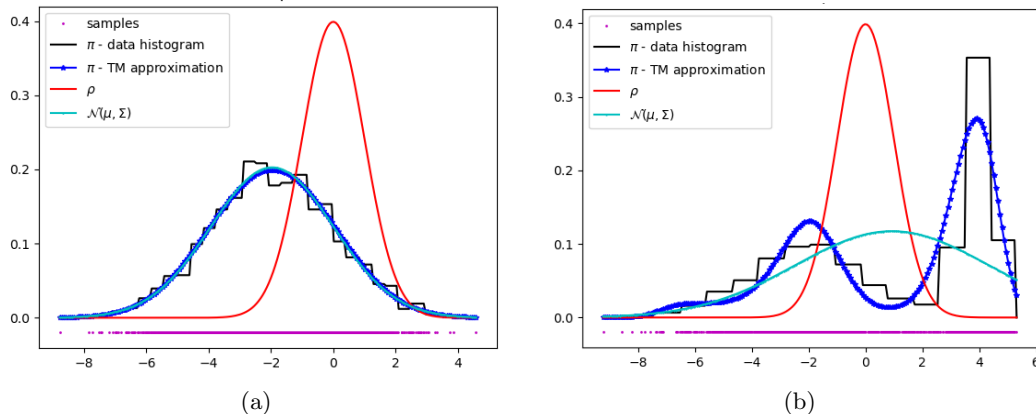


Figure 4: Approximations to univariate density functions via triangular transport maps. In each of the Subfigures 4a and 4b, (i) the red curve is the reference density ρ – a standard normal, (ii) a histogram of samples from the target density π is depicted with black lines, (iii) the blue curve is the transport map (TM) approximation to the target density π , and (iv) the cyan curve is the density for the normal distribution $\mathcal{N}(\mu, \Sigma)$ with mean and standard deviation being that of the sample data. For 4a, the data set was created by drawing samples from a normal distribution $\mathcal{N}(\mu, \Sigma)$ with $\mu \neq 0$ and $\Sigma \neq 1$. The TM approximation to the target density agrees with that of the true density. The samples for the data set from 4b are from a multi-modal distribution. The resulting TM approximation to the target density reflects this and follows the data histogram more closely, as opposed to the density for $\mathcal{N}(\mu, \Sigma)$.

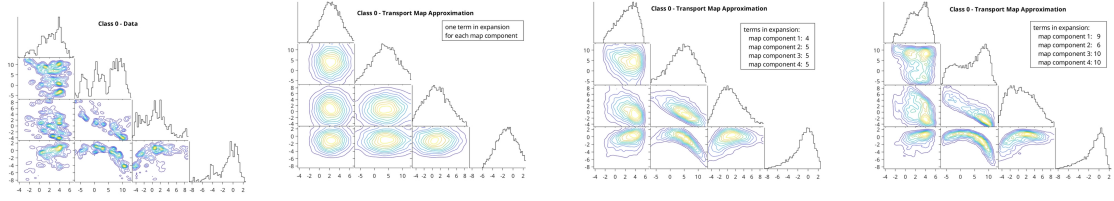
The figure shows how the measure transport framework can be used for uni-modal and multi-modal data distributions alike. Further details are provided in the caption for Figure 4.

Finally, transport map approximations to densities for a multivariate data set chosen from the UC Irvine Machine Learning Repository [18] appear in Figure 5. Although not from the biological domain, we selected the data set [20] because it yielded a good, non-contrived example for illustrating the benefits of a measure transport approach to density estimation. The data set was created from images taken from genuine and forged banknote-like specimens, creating two classes for classification problems. For the purpose of discussion, we identify them as class 0 and class 1 and compute approximations to the densities for each of the two classes. The triangular transport maps for the approximated densities were obtained using the AdaptiveTransportMaps library [3], which allows for computing adaptive parameterizations of transport maps [2].

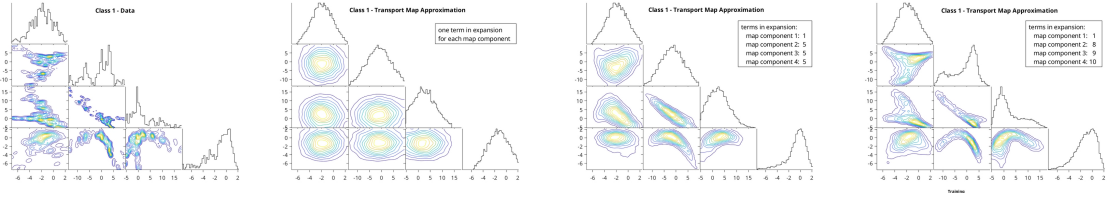
We provide a brief summary of the framework for such *adaptive transport maps* in Appendix A. Here we note that among the several parameters defining the adaptive transport maps is the number of terms in the basis function expansion for each map component. Figure 5 illustrates the effect of varying this allowed maximum number of terms and shows that, for each of the class 0 and class 1 data, increasingly good approximations to the density can be obtained. Classification results obtained via the transport map approximated density distribution functions are also shown. For comparison, classification results obtained using several Matlab classifiers [25] are included in Figure 5 as well.

5 Application to Gene Expression Data

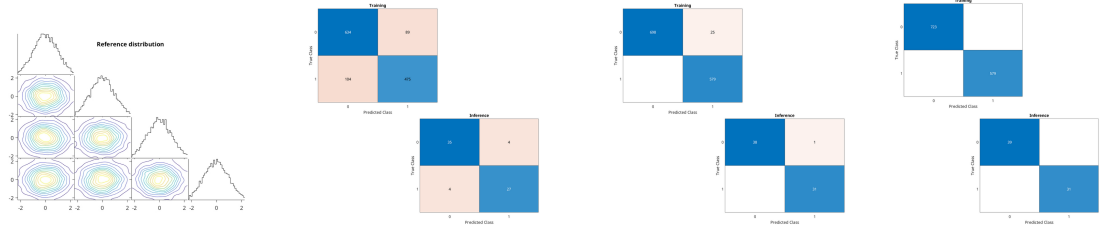
To conduct an initial assessment of the potential of measure transport techniques for phenotypic classification within the radiation biology domain, we use the GSE43151 data set [30] available from the Gene Expression Omnibus (GEO) database [9], as in previous work [22, 23]. This data set



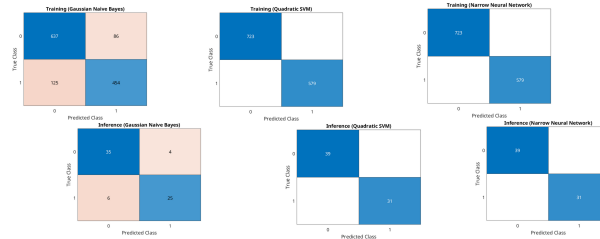
(a) Class 0



(b) Class 1



(c) Transport maps reference probability density (left) and confusion matrices corresponding to the classification results using the class-conditional density approximations from 5a and 5b



(d) Confusion matrices for naive Bayes (left), support vector machine (middle), and neural network (right) classification results

Figure 5: Transport map (TM) approximations to class-conditional densities for the data set [20]. *Subfigure 5a*: Class 0 marginal distribution densities from data (far left) and three different TM approximations, with an increasing number of terms in the basis function expansions for the TM components. Clearly, the data density distribution is not Gaussian. The first TM approximation, with only one term in each basis function expansion, approximates the target density poorly. The accuracy of the approximations improves with an increased number of terms in the basis function expansions. *Subfigure 5b*: As in Subfigure 5a, but for class 1. *Subfigure 5c*: Left: reference probability density, which is a standard multivariate normal for all TM approximations. Afterwards: improved classification result as the accuracy of the density approximations increases. The top row confusion matrices are from training data and the bottom row ones are from inference data. *Subfigure 5d*: As the data is not Gaussian, a naive Bayes classifier (left) performs poorly. A support vector machine (middle) and neural network (right) classifier perform as well as the classification resulting from the most accurate TMs approximation (far right, Subfigures 5a-5c).

contains gene expression data for 121 human blood samples, some with zero exposure to radiation, and others exposed to low-dose radiation or high-dose radiation. Out of the total number of samples, 18 are in the zero-dose category, 87 are in the low-dose category, and 16 are in the high-dose category. For more details on the GSE43151 data set, the reader may refer to [30]. The data set, as used in our experiments and the previous works [22, 23], is available from [21].

Genes correspond to the random variables jointly distributed according to the unknown target probability densities we seek to estimate. For feature (i.e., random variables) selection, we consider genes in biological pathways relevant to the GSE43151 data set, as determined by the pathway ranking procedure from [22, 23]. As previously mentioned in Section 4.1, we investigate two different measure transport techniques, namely, explicitly enforcing sparsity patterns in the transport maps and adaptive transport maps. Details appear in Section 5.1 for the former approach and in Section 5.2 for the latter one. In each case, the resulting transport maps are sparse, as defined towards the end of Section 4.1 and depicted in Figure 3.

As discussed next in Section 5.1 below, prior knowledge extracted from known biological pathways, such as relationships among genes, could be used to fix sets of active variables (i.e., sets of variables that the map components depend on) when computing the sparse transport maps. This is advantageous computationally, particularly if the extracted relationships are known with (reasonable) certainty. However, this approach could end up being biased and too restrictive (for example, missing possible dependencies between genes that are a priori unknown as well as obscuring their change when exposed to radiation). Hence, in Section 5.2, we also consider adaptive transport maps without any a priori imposed restrictions on the sparsity patterns of their components. With the latter class of maps, via specifically designed algorithms [2], sparse transport maps can be constructed and computed without the need to fix the set of active variables a priori. For our application, adaptive transport maps may thus offer more flexibility and would be more advantageous when prior knowledge about gene relationships is lacking or uncertain.

5.1 Prescribed Sparsity Patterns from Gene Relationships

One simple way to incorporate prior information into transport map construction is by building a sparse transport map using knowledge of the dependence structure of the set of random variables under consideration. If the random variables adhere to a Bayesian network, then the active variables of the transport map may be obtained from this network in a straightforward way [40]. In doing so, the number of parameters that need to be fit can be significantly reduced compared with triangular and dense maps.

For the gene expression data under radiation exposure, we used the Kyoto Encyclopedia of Genes and Genome (KEGG) database [16] to extract Bayesian networks describing the relationships between the genes for a given pathway. While KEGG provides a variety of relationships between genes, we focused on protein-protein (PPrel) activation and inhibition relationships. In particular, if there was a directed edge from gene A to gene B in the KEGG graph of type PPrel-activation/inhibition, then an edge from A to B was added to the Bayesian network. We also added edges between genes that are part of a gene complex. This information was extracted from KEGG Markup Language (KGML) files and read into Python using the BioPython package. We only consider pathways that resulted in directed acyclic graphs (DAGs) under these PPrel relationships. Software to extract this information is available from [15]. The transport maps for the experiments reported in this section were computed using the TransportMaps library [28], version 2.0b3.

To test out the performance of the sparse transport maps framework within this context, we selected 5 gene pathways from the KEGG database that performed well on the pathway activation scoring performed in [23] and resulted in DAGs as well, through the above analysis. We considered

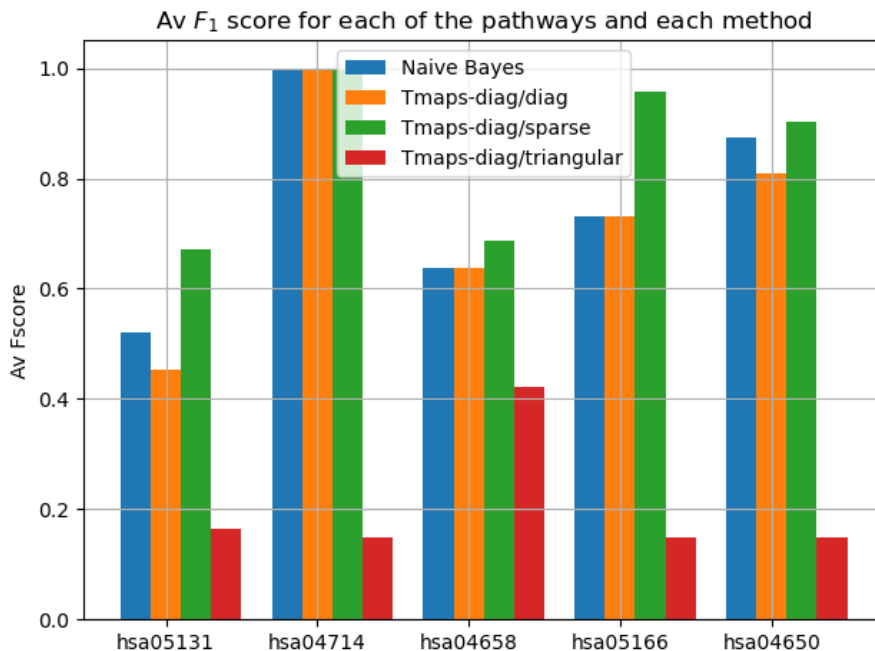


Figure 6: Classification results with KEGG-informed sparse transport map

the following pathways: hsa05131, hsa04714, hsa04658, hsa05166, and hsa04650. We performed the classification task of discriminating zero-dose versus low-dose samples using the subset of genes corresponding to each pathway. We were interested in the small-data regime where prior information can provide the biggest benefit, so we used only 25% of the data for the training set and the rest for evaluation, resulting in 25 training data samples and 80 test samples. Since there is so little data in the zero-dose case (only 4 training samples) it makes sense to use a diagonal transport map for this case, while other approaches performed poorly. In the low dose-case, there are 21 training samples and we consider using the following maps:

- *Diagonal map*: The i -th component of the transport map T^{-1} from equation (12) only depends on the value y_i of the i -th random variable \mathcal{Y}_i .
- *Dense triangular map*: The i -th component of the transport map T^{-1} depends on the values $\{y_j\}_{j=1}^i$ of the random variables $\{\mathcal{Y}_j\}_{j=1}^i$.
- *KEGG-informed sparse map*: The i -th component of the transport map T^{-1} depends on the value y_i of the random variable \mathcal{Y}_i and the values of a proper subset Z_i (possibly empty) of the random variables $\{\mathcal{Y}_j\}_{j=1}^{i-1}$. For the experiments reported here, $Z_i = \emptyset$ typically. The set of active variables for each map component is derived from biological prior knowledge in the form of a topological sort of the KEGG graph [15].

Refer to Figure 3 for a pictorial representation of the above listed types of maps. In each of the above cases, we have $T^{-1}: \mathbb{R}^m \rightarrow \mathbb{R}^m$, where m is the number of genes extracted from the pathway.

Figure 6 displays the F_1 score [35] averaged over both classes for each of the pathways and each method including Naive Bayes as a baseline. From the plot, we see that transport maps with the sparsity pattern derived from prior knowledge provides an improvement in performance across all pathways except one. Note the poor performance of the dense triangular map, which is unable to fit such a small amount of data.

5.2 Adaptive Transport Maps Approach

We now move on to adaptive transport maps [2], for which transport map sparsity patterns (i.e., the dependence structure of the set of random variables jointly distributed according to the target probability density) are not being prescribed a priori. First, we continue with classification experiments in Section 5.2.1 below. Afterwards, in Section 5.2.2 we discuss a different application which shows the potential of adaptive transport maps to serve as a tool for scientific discovery.

5.2.1 Further Classification Experiments

To design classification experiments using probability distribution densities approximated via adaptive transport maps (as opposed to Section 5.1 above, where transport maps sparsity patterns were prescribed *a priori*), we selected two pathways from the KEGG database [16], namely pathways hsa04120 and hsa05202. This was based on the pathway ranking procedure from [23], using the GSE43151 data set, where pathway hsa04120 ranked as the top pathway showing significant differential activation in response to low-dose radiation, as compared to zero-dose, and pathway hsa05202 ranked as the top pathway showing significant differential activation in response to high-dose radiation, as compared to zero-dose. After accounting for genes present in both the GSE43151 data set and in the selected pathways, we were left with 108 genes for pathway hsa04120 and 98 genes for pathway hsa05202.

Within the context of the classification problem from Section 2, we performed two groups of experiments. The first was for classifying samples between zero-dose (class 0) and low-dose (class 1) radiation, using the set of 108 genes common to both the GSE43151 data set and the hsa04120 pathway to define the set of random variables for the class-conditional densities. In the second group of experiments, classification was between zero-dose (class 0) and high-dose (class 1) radiation, using the set of 98 genes common to both the GSE43151 data set and the hsa05202 pathway as the set of random variables. For each of these two “class 0 - class 1 scenarios” we then decided on a number of maximum terms allowed in the basis function expansion for each map component (see the end of Section 4.2) and, given a maximum number of terms allowed (more on our choices later), a sequence of runs, say N of them, was carried out. For each of these runs:

1. A random ordering of the data samples from the GSE43151 data set was performed.
2. For each of class 0 and class 1, the first half of the samples from the resulting ordering was selected as a training data set and the second half was withheld for inference.
3. An adaptive transport map approximation to each class-conditional density was computed.
4. Classification was done, per (1), using the resulting class-conditional densities and the samples held for inference.
5. For comparison, classification was done with Matlab’s naive Bayes and support vector machine classifiers using the same training and inference data sets from item 2 above.

This is formally described in Algorithm 1, using the mathematical notation introduced previously in Section 3.

Results from the above described runs are summarized in the form of F_1 scores for the classification results. These are shown in Figure 7 for the case when class 0 and class 1 were set, respectively, as the zero-dose and low-dose radiation classes. For the zero-dose and high-dose classification scenario, results are summarized in Figure 8.

Algorithm 1 Classification experiments with adaptive transport maps

Notation:

N : number of runs

$m \geq 1$: number of genes in subset of genes extracted from GSE43151 data set

$y \in \mathbb{R}^m$: values (gene expression data) of a random vector $\mathcal{Y} = (\mathcal{Y}_1, \mathcal{Y}_2, \dots, \mathcal{Y}_m)$

K : number of classes

π_k : (unknown) target probability density for class $k \in \{0, \dots, K-1\}$

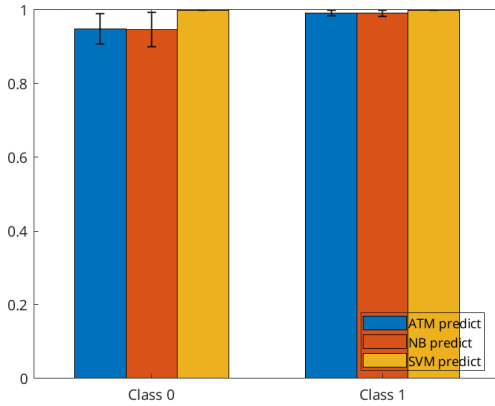
$Y_k = \{y \in \mathbb{R}^m : y \sim \nu_{\pi_k}\}$: set of all samples for class $k \in \{0, 1, \dots, K-1\}$

$n_k = \text{Card}(Y_k)$: number of samples in Y_k , $k \in \{0, 1, \dots, K-1\}$

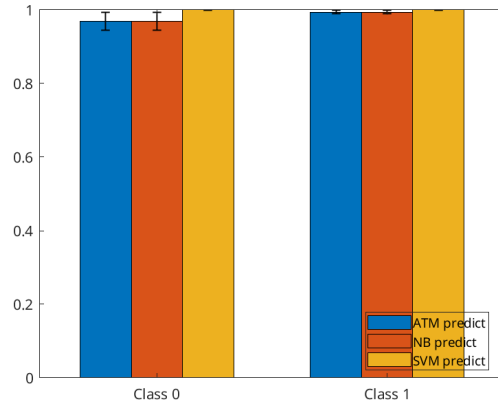
\mathcal{S}_{n_k} : group of permutations on n_k elements, acting on Y_k , with $\text{Card}(\mathcal{S}_{n_k}) = n_k!$

Algorithm:

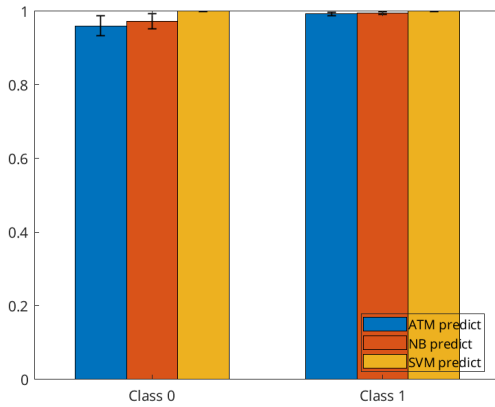
- 1: **for** $n = 1$ **to** N **do**
 - 2: **for each** $k \in \{0, 1, \dots, K-1\}$ **do**
 - 3: Choose an order on the set Y_k
 - 4: Choose randomly an element $\sigma \in \mathcal{S}_{n_k}$.
 - 5: Compute $\sigma(Y_k)$, i.e., act on Y_k by σ and reorder it.
 - 6: Split the set $\sigma(Y_k) = \sigma(Y_k)^{\text{tr}} \sqcup \sigma(Y_k)^{\text{inf}}$ along this order into a disjoint union of the set $\sigma(Y_k)^{\text{tr}}$ of its first $\lfloor \frac{n_k}{2} \rfloor$ elements (designated as training set) and the set $\sigma(Y_k)^{\text{inf}}$ of the remaining $n_k - \lfloor \frac{n_k}{2} \rfloor$ elements (designated as inference set).
 - 7: Compute an adaptive transport map approximation T_k from the reference ρ to the target density π_k using only $\sigma(Y_k)^{\text{tr}}$ as a training set. That is, T_k is computed to satisfy the condition $\nu_{\pi_k}(\sigma(Y_k)^{\text{tr}}) = \nu_{\rho}(T_k^{-1}(\sigma(Y_k)^{\text{tr}}))$. (cf. equation (2))
 - 8: **end for**
 - 9: **for each** $k \in \{0, 1, \dots, K-1\}$ **do**
 - 10: Compute $\hat{\pi}_k = \lfloor \frac{n_k}{2} \rfloor / \sum_{s=0}^{K-1} \lfloor \frac{n_s}{2} \rfloor$, the estimates for the class prior probabilities. (cf. equation (1))
 - 11: **end for**
 - 12: **for each** $k \in \{0, 1, \dots, K-1\}$ **do**
 - 13: **for each** $y \in \sigma(Y_k)^{\text{inf}}$ (the inference set) **do**
 - 14: Compute the probability $\Pr(C = k | \mathcal{Y} = y) = \hat{\pi}_k \pi_k(y) / \sum_{s=0}^{K-1} \hat{\pi}_s \pi_s(y)$ that sample y belongs to class k (cf. equation (1)), where $\pi_s(y)$ is estimated via equation (4) using the already computed (in step 7 above) transport map T_s , for each $s \in \{0, 1, \dots, K-1\}$.
 - 15: **end for**
 - 16: **end for**
 - 17: (Optional) For comparison, compute classification with Matlab's naive Bayes and support vector machine classifiers using the same training and inference data sets from line 6 (Algorithm 1).
 - 18: **end for**
-



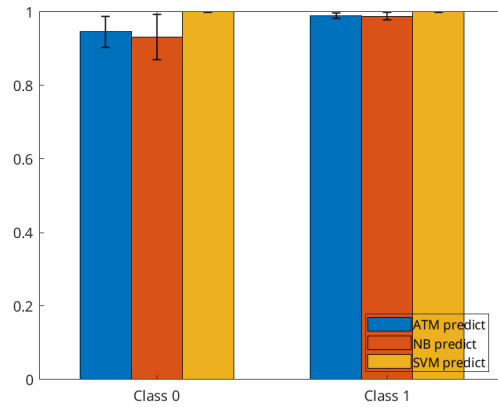
(a) Averaged F_1 scores, all experiments



(b) Averaged F_1 scores, subset of 20 experiments. Maximum number of terms allowed in ATM basis function expansions: 1 for class 0, 1 for class 1.



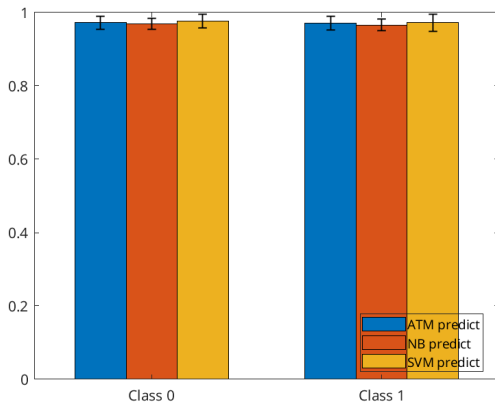
(c) Averaged F_1 scores, subset of 20 experiments. Maximum number of terms allowed in ATM basis function expansions: 2 for class 0, 5 for class 1.



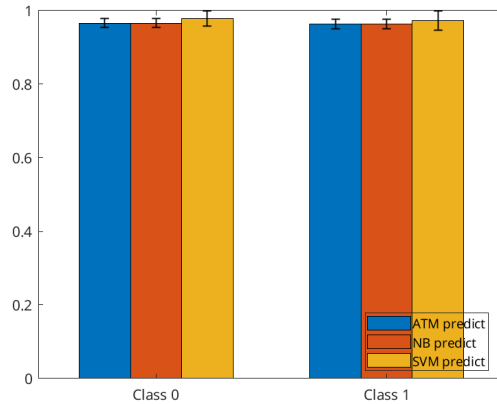
(d) Averaged F_1 scores, subset of 20 experiments. Maximum number of terms allowed in ATM basis function expansions: 2 for class 0, 6 for class 1.

Figure 7: Summary of classification results from adaptive transport maps (ATM) approximations to the class-conditional densities, naive Bayes (NB) classifier, and support vector machine (SVM) classifier. Zero-dose radiation is class 0; Low-dose radiation is class 1. The available number of samples were 18 for class 0 and 87 for class 1. For each experiment (i.e., run), the available samples were divided randomly into 50% for training and 50% for inference. The total number of experiments was 100. For this data set, all methods performed well, with SVM achieving perfect results in most experiments. On average, the classification results for the ATM density approximations and for naive Bayes were equal, as seen in Subfigure 7a. For disjoint subsets of experiments (Subfigures 7b-7d), the ATM and naive Bayes classifiers performed equally, or one slightly better than the other. For all experiments, classification results were more accurate for class 1. This is not surprising, since there were more data samples available for class 1.

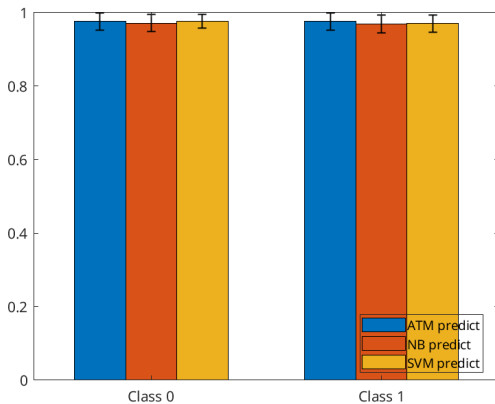
We note that for the experiments conducted, all classifiers ended up performing well. This was the case also in other preliminary experiments with the selected GSE43151 data set. A small number of terms (1-2 for the zero- and high-dose radiation classes; 1-6 for the low-radiation class) in the adaptive transport maps basis function expansions were sufficient for the approximations. Varying the maximum number of allowed terms in the transport maps basis function expansions did not yield appreciable differences in the results, contrary to the (non-biology) example from Figure



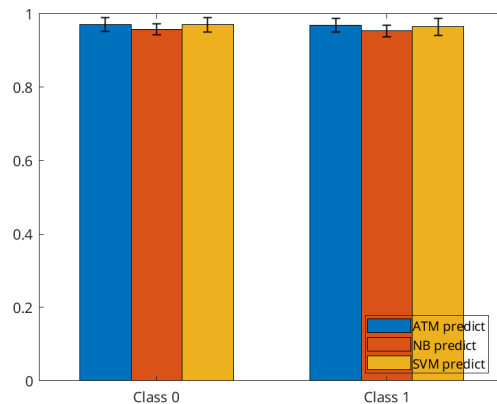
(a) Averaged F_1 scores, all experiments



(b) Averaged F_1 scores, subset of 20 experiments. Maximum number of terms allowed in ATM basis function expansions: 1 for class 0, 1 for class 1.



(c) Averaged F_1 scores, subset of 20 experiments. Maximum number of terms allowed in ATM basis function expansions: 2 for class 0, 1 for class 1.



(d) Averaged F_1 scores, subset of 20 experiments. Maximum number of terms allowed in ATM basis function expansions: 2 for class 0, 2 for class 1.

Figure 8: Summary of classification results from adaptive transport maps (ATM) approximations to the class-conditional densities, naive Bayes (NB) classifier, and support vector machine (SVM) classifier. Zero-dose radiation is class 0; High-dose radiation is class 1. The available number of samples were 18 for class 0 and 16 for class 1. For each experiment (i.e., run), the available samples were divided randomly into 50% for training and 50% for inference. The total number of experiments was 100. For this data set, all methods performed well, and nearly equal, on average. Classification scores were around the same for class 0 and class 1.

5. However, our experiments (as previous works from others) illustrate that the same measure transport framework can be used successfully (in practice) for diverse data sets.

5.2.2 Adaptive Transport Maps as a Tool for Scientific Discovery

As shown in the original publication [2], adaptive transport maps approximations can reveal (unknown) dependence structure among the set of random variables jointly distributed according to the target probability density. Thus, adaptive transport maps have the potential to serve as tools for scientific discovery. For our radiation biology application, a natural question would then be

whether the sparsity patterns resulting from the transport maps approximations to the target densities contain or reveal any biological information, for example, relationships between the genes associated with the transport map sparsity patterns. This is another task within the framework introduced in Section 2 (see Figure 1), independent of the classification problem, where the measure transport approach can have an impact.

For instance, the sparsity pattern shown in Figure 3b resulted from the computation of the transport maps needed for estimating the class-conditional density for low-dose radiation, using a subset of five genes from the GSE43151 data set as the random variables jointly distributed according to the target measure. From the sparsity pattern in Figure 3b, one question that arises naturally is whether within the radiation biology domain there are known relationships that correspond to the exhibited sparsity pattern, or whether there may exist unknown relationships, among the genes associated with random variables \mathcal{Y}_3 and \mathcal{Y}_4 or between the genes associated with the random variables \mathcal{Y}_1 , \mathcal{Y}_2 , \mathcal{Y}_3 and \mathcal{Y}_5 . Thus there is potential for hypotheses generation and subsequent expert verification. In addition, within the context of the computational workflow from Figure 1, the resulting sparsity patterns may conceivably be useful for designing queries (regarding gene relationships) for large language models as well [33, 34].

Now, given sufficient data samples, one can expect that sparsity patterns resulting from adaptive transport map density approximations to the data distribution will accurately uncover dependencies or associations hidden in the data. But even when data is scarce one may be able to use such sparsity patterns for hypotheses generation. Namely, one can gather statistics by computing many adaptive transport map density approximations using different (randomly selected) subsets of the data as training sets, and then identifying common dominating patterns appearing in the resulting collection of transport map sparsity patterns. We discuss this line of research next and in Figures 9–13, where results are shown from our computational experiments. In order to develop some intuition into the dependence structure of the genes from the GSE43151 data set, without assuming any knowledge that fixes the set of transport map active variables a priori, we consider a subset of six genes from the GSE43151 data set as the random variables jointly distributed according to the unknown target measure. That is, in what follows, $T^{-1} : \mathbb{R}^6 \rightarrow \mathbb{R}^6$ in equation (12). For reference, information about the selected subset of genes is provided in Table 1 and Figure 14, both appearing in Appendix B.

Recall from Figure 3 that in our pictorial representation of transport map sparsity patterns, the horizontal axis indexes the random variables $\{\mathcal{Y}_j\}_{j=1}^6$ and the vertical axis indexes the map components $\{(T^{-1})_i\}_{i=1}^6$. A square appears at the intersection of grid point (j, i) if the i -th map component $(T^{-1})_i$ depends on the value y_j of the j -th random variable \mathcal{Y}_j . For any given map component, the set of active variables is the set of random variables that the map component depends on. The active variables define a sparsity pattern for the transport map. We emphasize again that the adaptive transport map computation methods from [2] determine the set of active variables, without specification of it prior to computing the transport map.

Due to the small number of total samples available in the GSE43151 data set, sparsity patterns resulting from adaptive transport map approximations to the target measure may differ when different subsets of the total samples set are used to compute the transport maps. Figure 9 exemplifies this for the zero-dose and low-dose radiation classes. However, we hypothesize that statistics collected from various runs may nevertheless allow for uncovering information hidden in the data. The computations we perform to collect such statistics are described in Algorithm 2.

Namely, like in Algorithm 1 before, we work in Algorithm 2 with subsets (as training sets) extracted from the set of data samples after random permutations of the ordered set of GSE43151 data samples (see lines 8–10 of Algorithm 2). First, we fix an ordering $\sigma_p(\mathcal{Y}) = \left(\mathcal{Y}_{\sigma_p^{-1}(j)}\right)_{j=1}^6$ on

Algorithm 2 Gathering statistics from transport maps sparsity patterns

Notation:

- N : number of runs (transport maps) in a series of computations of transport maps
 $T_k^{(N,r)}$: r -th adaptive transport map computed in the series of N runs for Class k
 $m \geq 1$: number of genes in subset of genes extracted from GSE43151 data set
 σ_p : permutation on m elements, with inverse σ_p^{-1} , where $p \in \{1, 2, \dots, m!\}$
and $\sigma_1 = I$ is the identity permutation
 $\sigma_p(\mathcal{Y})$: result of the action of σ_p on the vector $\mathcal{Y} = (\mathcal{Y}_1, \dots, \mathcal{Y}_m)$ of random variables, for which $\sigma_p(\mathcal{Y}) = \left(\mathcal{Y}_{\sigma_p^{-1}(j)}\right)_{j=1}^m$ (cf. Table 2 from Appendix B)
 $z \in \mathbb{R}^m$: values (gene expression data) of a random vector $\mathcal{Z} \equiv \sigma_p(\mathcal{Y})$
 K : number of classes
 π_k : (unknown) target probability density for Class $k \in \{0, \dots, K-1\}$
 $Z_k = \{z \in \mathbb{R}^m : z \sim \nu_{\pi_k}\}$: set of all samples for class $k \in \{0, 1, \dots, K-1\}$
 $n_k = \text{Card}(Z_k)$: number of samples in Z_k , $k \in \{0, 1, \dots, K-1\}$
 \mathcal{S}_{n_k} : group of permutations on n_k elements, acting on Z_k , with $\text{Card}(\mathcal{S}_{n_k}) = n_k!$
 $B_k^{(N,\sigma_p)}$: $m \times m$ lower triangular matrix storing frequency counts from sparsity patterns for N transport maps computed for class k and permutation $\sigma_p(\mathcal{Y})$

Algorithm:

- 1: Choose (at random) a permutation $\sigma_p \in \mathcal{S}_m$ on m elements. ▷ see Table 2
 - 2: Let $(\mathcal{Z}_1, \mathcal{Z}_2, \dots, \mathcal{Z}_m) \equiv \sigma_p(\mathcal{Y})$
 - 3: **for** $r = 1$ **to** N **do**
 - 4: **for each** $k \in \{0, 1, \dots, K-1\}$ **do**
 - 5: Initialize $B_k^{(N,\sigma_p)}$ to the $m \times m$ (lower triangular) zero matrix.
 - 6: **end for**
 - 7: **for each** $k \in \{0, 1, \dots, K-1\}$ **do**
 - 8: Choose randomly an element $\sigma \in \mathcal{S}_{n_k}$.
 - 9: Compute $\sigma(Z_k)$, i.e., act on Z_k by σ and reorder it.
 - 10: Split the set $\sigma(Z_k) = \sigma(Z_k)^{\text{tr}} \sqcup \sigma(Z_k)^{\text{inf}}$ along this order into a disjoint union of the set $\sigma(Z_k)^{\text{tr}}$ of its first $\lfloor \frac{n_k}{2} \rfloor$ elements (designated as training set) and the set $\sigma(Z_k)^{\text{inf}}$ of the remaining $n_k - \lfloor \frac{n_k}{2} \rfloor$ elements (designated as inference set).
 - 11: Compute an adaptive transport map approximation $T_k^{(N,r)}$ from the reference ρ to the target density π_k using only $\sigma(Z_k)^{\text{tr}}$ as a training set. That is, $T_k^{(N,r)}$ is computed to satisfy the condition
$$\nu_{\pi_k}(\sigma(Z_k)^{\text{tr}}) = \nu_{\rho} \left(\left(T_k^{(N,r)} \right)^{-1} \left(\sigma(Z_k)^{\text{tr}} \right) \right). \text{ (cf. equation (2))}$$
 - 12: **for** $j = 1$ **to** m **do**
 - 13: **for** $i = 1$ **to** j **do**
 - 14: **if** i -th component of $\left(T_k^{(N,r)} \right)^{-1}$ depends on the value of the
 - 15: j -th random variable \mathcal{Z}_j (cf. Figures 3, 9) **then**
 - 16: $B_k^{(N,\sigma_p)}(j, i) = B_k^{(N,\sigma_p)}(j, i) + 1$ ▷ increase frequency count
 - 17: **end if**
 - 18: **end for**
 - 19: **end for**
 - 20: **end for**
 - 21: **end for**
-

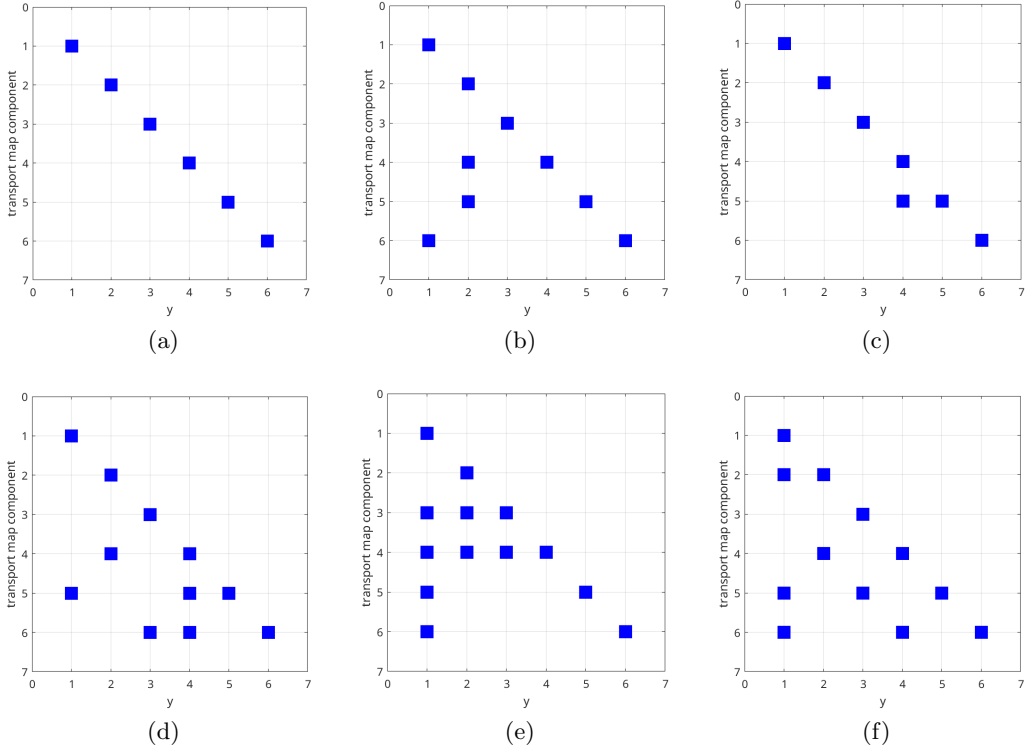


Figure 9: Due to the small number of total samples available, resulting transport map sparsity patterns may differ when different training subsets of the total samples set are used to compute adaptive transport maps. Subfigures 9a–9c exemplify this for three select subsets (of 9 samples each) from the zero-dose radiation class. Similarly for the low-dose radiation class in Subfigures 9d–9f, where each subset had 44 samples when computing the corresponding adaptive transport map. Statistics collected from various runs may nevertheless allow for uncovering information hidden in the data, as shown in Figures 10–13.

the set $\{\mathcal{Y}_j\}_{j=1}^6$ of random variables (i.e., we fix an ordering on the arguments of the transport maps to be computed), where $\sigma_p \in \mathcal{S}_6$ – the permutation group on six ($m = 6$) elements. Recall that we consider only triangular maps throughout (see equations 10–12). We restrict our attention to only two ($K = 2$) classes: the zero-dose ($k = 0$) and low-dose ($k = 1$) radiation classes. For each class $k \in \{0, 1\}$ and a given number N , we compute a series $\{T_k^{(N,r)}\}_{r=1}^N$ of transport maps $T_k^{(N,r)} : \mathbb{R}^6 \rightarrow \mathbb{R}^6$, $r = 1, \dots, N$, rendering approximations $\pi_k^{(N,r)}$ to the target density π_k on \mathbb{R}^6 describing the joint density distribution of the six random variables $\{\mathcal{Y}_j\}_{j=1}^6$ in question. More precisely, for each class $k \in \{0, 1\}$ we performed five *independent* computations of series $\{T_k^{(N,r)}\}_{r=1}^N$ of transport maps with a number of maps (runs) $N = 10, 20, 50, 100, 200$ in each, respectively, and with the same fixed order $\sigma_p(\mathcal{Y})$ of the random variables.

We observed that for each class $k \in \{0, 1\}$ (and more so with an increasing N) the elements in the series $\{T_k^{(N,r)}\}_{r=1}^N$ cluster around a map \bar{T}_k the components $\{(\bar{T}_k^{-1})_i\}_{i=1}^6$ of whose inverse show a particular persistent and dominant pattern of dependence on its arguments (active variables), referred to previously as the sparsity pattern (see Figure 3 for the definition). In order to exhibit this pattern quantitatively, for each of the zero-dose and low-dose radiation classes, we recorded the frequency with which each random variable in $\{\mathcal{Y}_j\}_{j=1}^6$ appeared as an active variable in the components $\{((T_k^{(N,r)})^{-1})_i\}_{i=1}^6$, separately within each of the five independently computed series

$\{T_k^{(N,r)}\}_{r=1}^N$ of adaptive transport maps, for $N = 10, 20, 50, 100, 200$ as explained above. This corresponds to lines 14–17 in Algorithm 2. Using these frequency counts we then constructed an “aggregated” sparsity pattern for each of the five series $\{T_k^{(N,r)}\}_{r=1}^N$, $N = 10, 20, 50, 100, 200$, for each one of the two classes $k \in \{0, 1\}$. Results are shown in Figures 10 and 11, respectively, for the zero-dose and low-dose radiation classes. To simplify notation, whenever there is no danger of confusion, in what follows we drop the subscript k and superscript (N, r) in the transport map notation $T_k^{(N,r)}$ introduced above and in Algorithm 2.

To explain the pictorial representation of such “aggregated” sparsity patterns, let’s take one subfigure from Figure 10, for example, Subfigure 10a. Note the grid point ordering on the plot axes: left to right for the horizontal axis, indexing the random variables $\{\mathcal{Y}_j\}_{j=1}^6$, and top to bottom for the vertical axis, indexing the map components $\{(T^{-1})_i\}_{i=1}^6$. The plot color bar ranges from 1 to the number N , which in this case is 10. Since, for each $i = 1, \dots, 6$, the i -th map component $(T^{-1})_i$ must depend on the value y_i of the i -th random variable \mathcal{Y}_i , and we are aggregating results for 10 computed transport maps, the frequency count depicted on each of the diagonal grid points is 10. Thus, each square on a diagonal grid point is identified with the highest frequency count, per the color bar. Out of the 10 transport maps computed, three resulted with the 4-th map component having dependence on the value y_2 of the random variable \mathcal{Y}_2 . Hence the square at grid point (2,4) is identified with a frequency count of 3, per the color bar. Similarly, two out of the 10 transport maps resulted with dependence on the value y_1 of the random variable \mathcal{Y}_1 for the 6-th map component and therefore the square at grid point (1,6) is identified with a frequency count of 2. Finally, there were three instances of aggregated dependence with frequency count of 1. These are identified by the white squares (lowest frequency count per the color bar) appearing at grid points (1,5), (1,2), and (4,5).

Computing frequency counts for (independently computed) larger collections of transport maps, as in Figures 10a–10e for the zero-dose radiation class and Figures 11a–11e for the low-dose one, we observe that patterns of high-valued frequency counts (pointing to particular subsets of random variables) start to emerge and persist. We note that a larger collection of transport maps need not contain the smaller previously independently computed collection of transport maps, for, as we know from the description of Algorithm 2, the computation of each transport map uses as a training set a randomly selected subset of the set of all available samples for the given class – that is indeed the case in Figures 10 and 11.

In order to verify robustness of the results with respect to changes in the ordering of the random variables, the computational experiments described via Figures 10–11 were repeated using 20 different permutations $\{\sigma_p(\mathcal{Y})\}_{p=1}^{20}$ of the ordered set $\mathcal{Y} \equiv (\mathcal{Y}_j)_{j=1}^6$ of random variables. The different permutations used are listed in Table 2, appearing in Appendix B. Details about the experiments for each of the permutations are provided in Appendix B. Here we note that the persistence of patterns of high-valued frequency counts resulting from the computational experiments, as described in Figures 10–11, and which correspond to the identity permutation $\sigma_1(\mathcal{Y})$ case, was also observed in the case of each of the 19 permutations $\{\sigma_p(\mathcal{Y})\}_{p=2}^{20}$.

We thus take the results from the case of $N = 200$ runs (*cf.* Figures 10e and 11e) for each of the 20 permutations $\{\sigma_p(\mathcal{Y})\}_{p=1}^{20}$, and map them to the random variable ordering corresponding to the identity permutation $\sigma_1(\mathcal{Y})$, so that we can report the aggregated results for these 4,000 runs. This is summarized in Figures 12–13. The resulting high-valued frequency counts in the sparsity patterns are suggestive of gene relationships encoded (or hidden) in the data which, as we have already mentioned, may aid in hypothesis generation for subsequent validation.

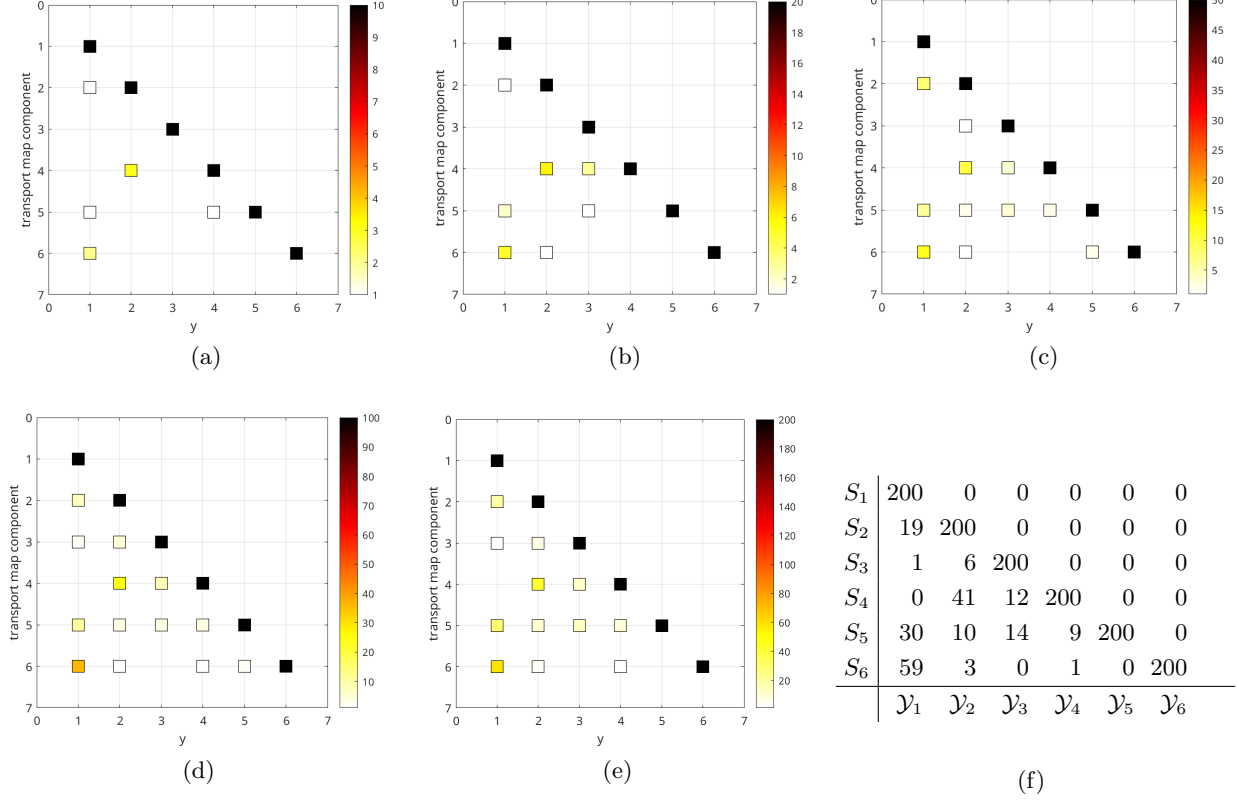


Figure 10: Aggregated sparsity patterns from adaptive transport map approximations to data distributions for different subsets of the zero-dose radiation data samples. The permutation on the ordered set $\mathcal{Y} \equiv (\mathcal{Y}_j)_{j=1}^6$ of random variables for the computational experiments summarized in Subfigures 10a–10f is the identity permutation $\sigma_1(\mathcal{Y}) = (\mathcal{Y}_1 \mathcal{Y}_2 \mathcal{Y}_3 \mathcal{Y}_4 \mathcal{Y}_5 \mathcal{Y}_6)$ (see Table 2 from Appendix B). Subsets of samples consisting of half the number of total samples (which for the zero-dose radiation class is 18) were generated from random permutations of the GSE43151 data set sample ordering. In Subfigures 10a, 10b, 10c, 10d, and 10e are represented the sparsity patterns corresponding to, respectively, 10, 20, 50, 100, and 200 such sample subsets. By aggregating results for increasing numbers of sample subsets, patterns of high-valued frequency counts are seen to emerge and persist. The groups of runs represented in Subfigures 10a–10e were independent, so low-valued frequency counts in the sparsity patterns need not persist as we move from Subfigure 10a to Subfigure 10e. This was the case for grid point (5,6) in Subfigures 10d and 10e, which shows a frequency count of two on the value y_5 of the random variable \mathcal{Y}_5 for map component S_6 in Subfigure 10d, but a frequency count of zero in Subfigure 10e. For reference, Subfigure 10f shows the frequency counts corresponding to the sparsity pattern from Subfigure 10e. In other words, the matrix shown in Subfigure 10f is the matrix $B_0^{(200, \sigma_1)}$ from Algorithm 2, lines 12–19. To simplify notation in Subfigure 10f, we denote $S \equiv T^{-1}$ for the inverse T^{-1} of a transport map T .

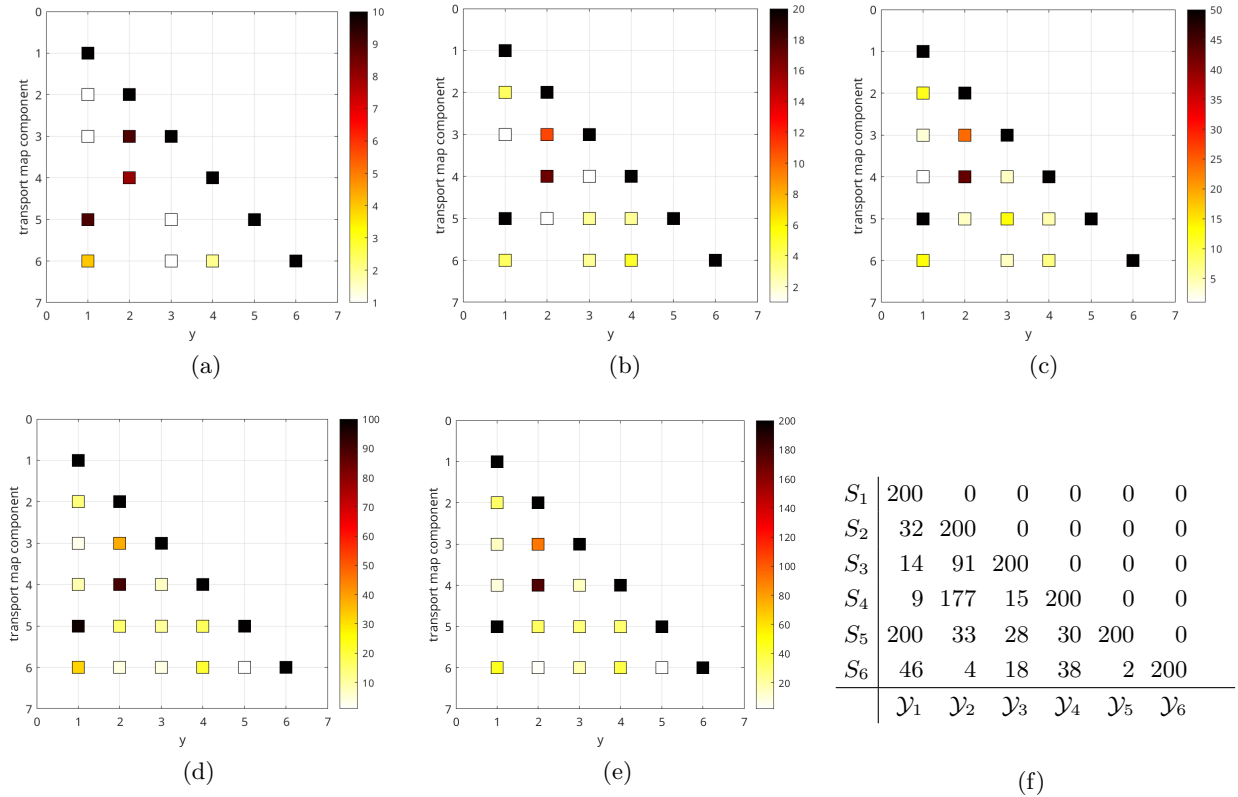
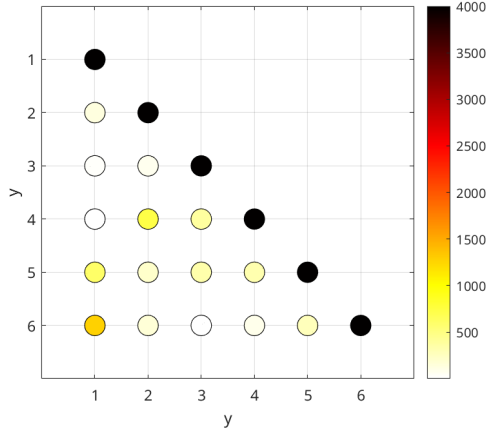
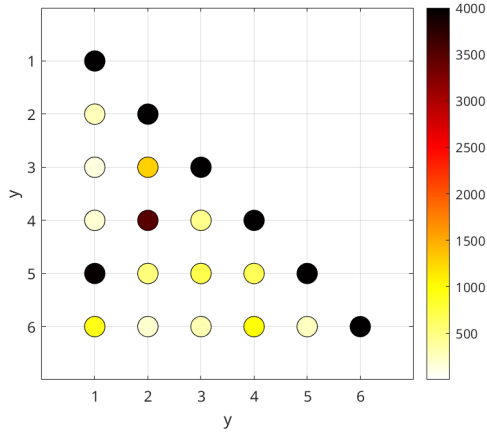


Figure 11: Aggregated sparsity patterns from adaptive transport map approximations to data distributions for different subsets of the low-dose radiation data samples. The permutation on the ordered set $\mathcal{Y} \equiv (\mathcal{Y}_j)_{j=1}^6$ of random variables for the computational experiments summarized in Subfigures 10a–10f is the identity permutation $\sigma_1(\mathcal{Y}) = (\mathcal{Y}_1 \mathcal{Y}_2 \mathcal{Y}_3 \mathcal{Y}_4 \mathcal{Y}_5 \mathcal{Y}_6)$ (see Table 2 from Appendix B). Subsets of samples consisting of half the number of total samples (which for the low-dose radiation class is 87) were generated from random permutations of the GSE43151 data set sample ordering. In Subfigures 11a, 11b, 11c, 11d, and 11e are represented the sparsity patterns corresponding to, respectively, 10, 20, 50, 100, and 200 such sample subsets. As for the zero-dose radiation class in Figure 10, by aggregating results for increasing numbers of sample subsets, patterns of high-valued frequency counts are seen to emerge and persist. For reference, Subfigure 11f shows the values of the frequency counts corresponding to the sparsity pattern from Subfigure 11e. In other words, the matrix shown in Subfigure 11f is the matrix $B_1^{(200, \sigma_1)}$ from Algorithm 2, lines 12–19. To simplify notation in Subfigure 11f, we denote $S \equiv T^{-1}$ for the inverse T^{-1} of a transport map T .



(a) zero-dose radiation class

\mathcal{Y}_1	4000	0	0	0	0	0
\mathcal{Y}_2	132	4000	0	0	0	0
\mathcal{Y}_3	20	69	4000	0	0	0
\mathcal{Y}_4	10	721	386	4000	0	0
\mathcal{Y}_5	600	212	337	321	4000	0
\mathcal{Y}_6	1273	160	1	85	279	4000
	\mathcal{Y}_1	\mathcal{Y}_2	\mathcal{Y}_3	\mathcal{Y}_4	\mathcal{Y}_5	\mathcal{Y}_6

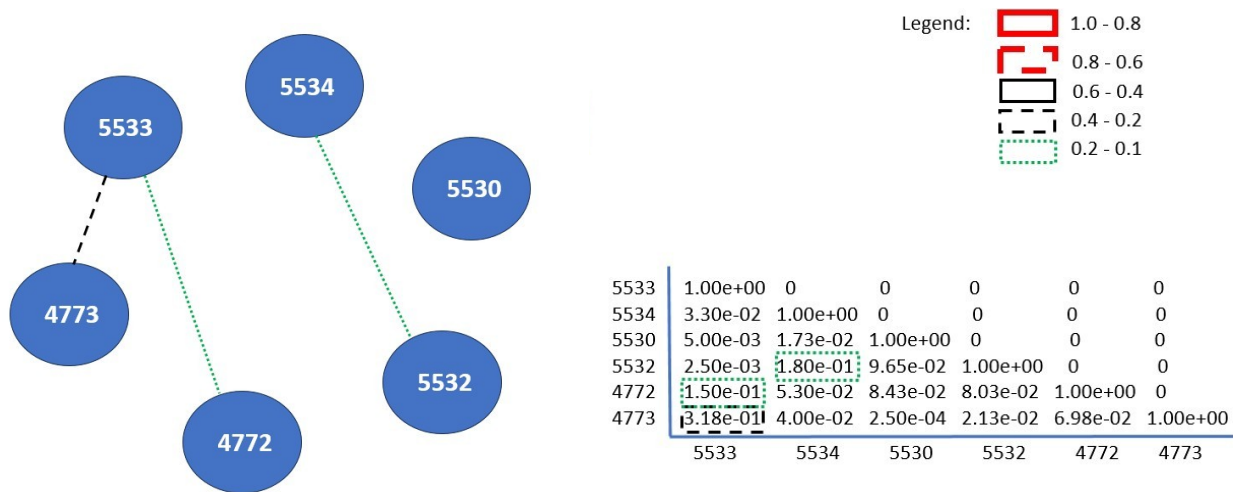
(b) $Q_0^{(4000)}$ 

(c) low-dose radiation class

\mathcal{Y}_1	4000	0	0	0	0	0
\mathcal{Y}_2	277	4000	0	0	0	0
\mathcal{Y}_3	137	1275	4000	0	0	0
\mathcal{Y}_4	185	3486	455	4000	0	0
\mathcal{Y}_5	3966	529	712	661	4000	0
\mathcal{Y}_6	922	203	313	985	258	4000
	\mathcal{Y}_1	\mathcal{Y}_2	\mathcal{Y}_3	\mathcal{Y}_4	\mathcal{Y}_5	\mathcal{Y}_6

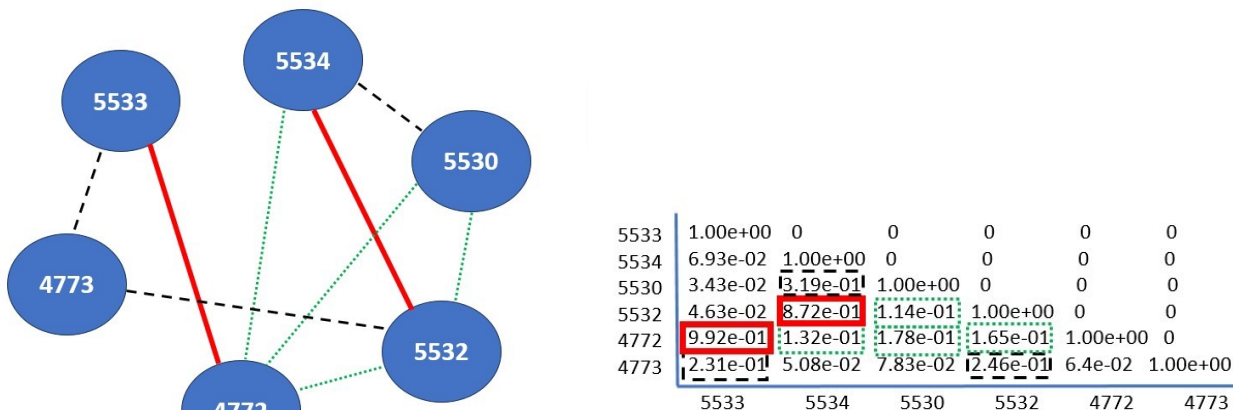
(d) $Q_1^{(4000)}$

Figure 12: *Subfigures 12a–12b*: Frequency counts gathered (see Appendix B) from sparsity patterns of adaptive transport map approximations to data distributions for different subsets of the zero-dose radiation data samples. *Subfigures 12c–12d*: As in Subfigures 12a–12b, but for the low-dose radiation data samples. The above subfigures report the results obtained by executing Algorithm 2 for each of the 20 different permutations $\{\sigma_p(\mathcal{Y})\}_{p=1}^{20}$ listed in Table 2 from Appendix B, specifically for the case $N = 200$ (*cf.* Figures 10e and 11e; also Algorithm 2). To account collectively for the number of 4,000 runs summarized in the above subfigures, the results obtained for each of the permutations $\{\sigma_p(\mathcal{Y})\}_{p=1}^{20}$ were mapped to random variable ordering corresponding to the identity permutation $\sigma_1(\mathcal{Y})$, as described in Algorithm 3. Specifically, the matrices shown in Subfigures 12b and 12d resulted from line 18 of Algorithm 3. The random variable to gene ID mapping is $(\mathcal{Y}_1 \ \mathcal{Y}_2 \ \mathcal{Y}_3 \ \mathcal{Y}_4 \ \mathcal{Y}_5 \ \mathcal{Y}_6) \mapsto (5533 \ 5534 \ 5530 \ 5532 \ 4772 \ 4773)$. (Refer to Tables 1 and 2 from Appendix B.) Dependencies/relations among genes suggested by the above results are further depicted in Figure 13.



(a) zero-dose radiation class

(b) $Q_0^{(4000)}$, as a fraction of a total number 4,000 of runs



(c) low-dose radiation class

(d) $Q_1^{(4000)}$, as a fraction of a total number 4,000 of runs

Figure 13: *Subfigures 13a-13b*: Dependencies among the genes for the zero-dose radiation class, as implied by the sparsity pattern from Figure 12a and the associated frequency counts from Figure 12b. *Subfigures 13c-13d*: Dependencies among the genes for the low-dose radiation class, as implied by the sparsity pattern from Figure 12c and the associated frequency counts from Figure 12d. Information about the subset of six genes selected for the computational experiments, including the gene IDs, appears in Table 1 from Appendix B. The entries in the tables shown in Subfigures 13b and 13d above contain, respectively, the frequency counts from Figures 12b and 12d as a fraction of a total number of 4,000 runs, and mapped to the gene IDs. These fractional values and the (user defined) thresholds from the legend at the top right corner of Subfigure 13b are used in the above figures to represent a “strength” of the relationship between genes, as implied by the adaptive transport maps sparsity patterns from Figures 12a and 12c. A natural question is whether the above reveal biological information, such as relationships among genes with no radiation exposure that change (appear, disappear) or persist upon exposure to low-dose radiation.

6 Discussion

As mentioned in Section 1, one among several advantages of measure transport methods is that they allow for a unified framework for processing and analysis of data distributed according to a wide range of probability measures. This powerful property is one of the reasons why measure transport techniques are active areas of research up to the present day, despite the fact that the subject itself has a long history. A framework for probability density estimation supported by measure transport techniques clearly offers benefits for many applications, including those in biology. For instance, recent work by [7] has shown that improved interpretation of cancer transcriptomic data can result by accounting for differences in the distribution densities of gene expressions. This is just one example where a framework for probability distribution density estimation, grounded on measure transport methods, could have significant impact.

Specific to the present manuscript, one of the ultimate goals when studying the GSE43151 data set is to understand the global dependence structure between the genes represented there through their expression data interpreted as a set of values of a set of random variables with a joint d -variate probability density Π_k on \mathbb{R}^d , where d denotes the number of genes in the data set, and $k \in \{0, 1, \dots, K - 1\}$ labels the different radiation level classes. The GSE43151 data set we used (available from [21]) contains samples for $d = 10,874$ genes. The approach and methods we presented here (which are inclusive of, although not exclusively for, scarce data scenarios) are very general and to our knowledge have not been pursued in the biology domain. (We note, however, that application of other measure transport methods in the biology domain appear in the literature – for example, see [43, 6, 13] for neural network and optimal transport applications.) Combined with present day computational capabilities, such an approach renders the task of achieving goals as the above feasible.

For instance, within this framework, the computations and results from Section 5.2.2 can be viewed as follows. Choosing a subset of m genes (where $m = 6$ genes were considered in Section 5.2.2) we essentially chose a subspace $\mathbb{R}^m \subset \mathbb{R}^d$ and, by computing triangular transport maps $T_k : \mathbb{R}^m \rightarrow \mathbb{R}^m$, estimated target probability densities π_k on \mathbb{R}^m which can be thought of as approximations of m -variate marginals of the (unknown) global d -variate probability densities Π_k . In other words, we chose a (known) projection $P : \mathbb{R}^d \rightarrow \mathbb{R}^m$ and estimated the marginals $\nu_{\pi_k} = P_{\#}\nu_{\Pi_k}$ (transports of ν_{Π_k} along this projection) on \mathbb{R}^m by constructing triangular transport maps satisfying $\nu_{\pi_k} = (T_k)_{\#}\nu_{\rho}$, where the reference probability density ρ on \mathbb{R}^m was chosen to be an m -variate Gaussian.

The dependence structure between genes in this small subset (as implied by the computed estimates to the probability distribution densities) was then uncovered by analyzing the sparsity patterns exhibited by the computed triangular transport maps. In general, assuming that \mathbb{R}^d is equipped with a reference Gaussian measure ν_{Γ} , one may address the question of computing global triangular transport maps $\mathcal{T}_k : \mathbb{R}^d \rightarrow \mathbb{R}^d$, satisfying $\nu_{\Pi_k} = (\mathcal{T}_k)_{\#}\nu_{\Gamma}$ and estimating the (unknown) global probability density Π_k , where Γ is a d -variate Gaussian reference probability density. It will be interesting to understand the sparsity patterns of the global maps \mathcal{T}_k , as their structure will reveal dependencies and strength of correlations between different genes represented in the entire data set.

Note that such an insight should reveal known and unknown information about pathways as well, since pathway information should be encoded into the dependency structure of the global target probability densities Π_k and therefore in the sparsity patterns of the global triangular transport maps \mathcal{T}_k . As already mentioned, in Section 5.2 we do not assume *a priori* any particular structure of the gene network. For example, graphs that represent (portions of) a gene network are not acyclic, in general. Thus, our method and analysis from Section 5.2.2 is not restricted a priori to

directed acyclic graphs assumed to represent gene regulatory networks.

The results of adopting this general approach are already seen in Figure 13, where emerging complex relations can be observed in the low-dose radiation class within the small subset of six genes (i.e., random variables) that we studied in detail. Whether to ignore or not the impact of possible feedback loops in the gene network, as well as the overall interpretation of the relationships among genes uncovered from the transport maps sparsity patterns, will depend on an external expert knowledge and judgment. Extracting local information by estimating the triangular transport maps T_k and target densities π_k on a subset of genes and/or using an already established knowledge about the relations between genes within a subset (for example, a pathway known with certainty, which will predetermine the sparsity pattern of local transport maps and the dependency structure of local target probability densities) can help in computing the global transport maps \mathcal{T}_k and estimating target densities Π_k . Namely, this prior knowledge can be incorporated into the original mathematical problem (i.e., first equation in the system (15) below) as added constraints:

$$\begin{aligned} \nu_{\Pi_k} &= (\mathcal{T}_k)_{\#} \nu_{\Gamma} \\ (T_k)_{\#} (P_{\#} \nu_{\Gamma}) &= P_{\#} ((\mathcal{T}_k)_{\#} \nu_{\Gamma}) \\ &\vdots \end{aligned} \tag{15}$$

where the local map T_k has been computed already and the second equation in the system (15) above (i.e., constraint for the global triangular transport map \mathcal{T}_k) follows from the commutativity condition $T_k \circ P = P \circ \mathcal{T}_k$.

Furthermore, the results depicted in Figure 13 suggest a certain “dynamics” on the space of transport maps (reflected in the changes to their sparsity patterns), as the level of radiation for class $k \in \{0, 1, \dots, K - 1\}$ changes, revealing also changes in correlations between genes in the subset of genes under consideration. Moreover, as described in [30], one could gather gene expression data within a fixed class $k \in \{0, 1, \dots, K - 1\}$ at different instances of time $t = t_1, t_2, \dots, t_n$ after an irradiation with a certain dose (labeled by the class k) has occurred. In other words, one observes the time dynamics on the space of random variables $\mathcal{Y}(t) = (\mathcal{Y}_1(t), \mathcal{Y}_2(t), \dots, \mathcal{Y}_d(t)) \in \mathbb{R}^d$, which implies time dynamics on the space of target probability measures $\nu_{\Pi_k}(t)$ (or equivalently, on the space of target probability densities $\Pi_k(t)$), which itself induces time dynamics on the space of triangular transport maps $\mathcal{T}_k(t)$ estimating the latter, all within the class k .

Using such time-dependent gene expression data, one can compute then a sequence of triangular transport maps $\{\mathcal{T}_k(t_l)\}_{l=1}^n$, and use them as validation points for a stochastic model describing the dynamics of $\mathcal{T}_k(t)$ and thus the correlation time dynamics of the entire gene network after a radiation dose has been applied. Of course, all of the above could be done locally if one restricts the study to a subset of genes, that is, to the time dynamics of a subset of random variables $\mathcal{Y}(t) = (\mathcal{Y}_1(t), \mathcal{Y}_2(t), \dots, \mathcal{Y}_m(t)) \in \mathbb{R}^m \subset \mathbb{R}^d$ and the corresponding local target probability measure $\nu_{\pi_k}(t)$ (or target probability density $\pi_k(t)$), and the estimating local triangular transport map $T_k(t)$.

In summary, the work reported in this manuscript shows some of the benefits that measure transport techniques will provide as part of the computational workflow from Section 2, intended to support research in the biological sciences. In domains for which data scarcity is common, such as in the radiation biology case study from Section 5, engagement with domain scientists will aid in identifying types of prior knowledge (in addition to biological pathway knowledge) which can be incorporated into the formulation of the mathematical problems being solved. This should allow to better account for the scarcity of training data. How to incorporate prior knowledge will obviously depend on the type of prior knowledge and problem being addressed but, generally, we mention feature selection for model training as well as incorporation of additional constraints in optimization problems being solved as common approaches.

Immediate tasks to pursue, in collaboration with domain scientists, include generation of synthetic data sets that will allow design of more controlled computational experiments with the goal of gaining a better (quantitative) understanding of the dependence of the methodologies proposed in Section 5.2 on the amount of data available for training. This will aid in carrying out a formal mathematical analysis of the method proposed in Section 5.2.2 as well. Additional (non-synthetic) data sets for validation of the proposed methodologies also will be sought.

Acknowledgements

This work was supported by the U.S. Department of Energy, Office of Science, RadBio program under Award KP1601011/FWP CC121. VLM thanks Francis J. Alexander who, as a RadBio PI, supported the measure transport approach, as well as for helpful discussions while the research was being carried out. VLM also thanks Ognyan Stoyanov for helpful discussions on measure transport theory and for very useful feedback on preliminary versions of this manuscript, Ricardo Baptista for helpful discussions on adaptive transport maps and the TransportMaps library, Daniel Sharp for helpful discussions on the MParT library, and Shinjae Yoo and Shantenu Jha for some managerial assistance.

A Appendix: Adaptive Transport Maps Framework

The computational transport maps framework proposed by [2], termed *adaptive transport maps* by the authors, and which we use in the present manuscript in Section 5.2 and the example from Figure 5 of the main text as well, is outlined next. For technical details, the reader is referred to the original publication [2] and references therein.

Recall from Section 4.1 of the main text that a transport map $T : \mathbb{R}^m \rightarrow \mathbb{R}^m$, such that $\nu_\pi = T_\# \nu_\rho$, is triangular if the i -th component T_i of T only depends on the values $\{x_j\}_{j=1}^i$ of the first i random variables $\{\mathcal{X}_j\}_{j=1}^i$:

$$T(x) = \begin{bmatrix} T_1(x_1) \\ T_2(x_1, x_2) \\ \vdots \\ T_m(x_1, x_2, \dots, x_m) \end{bmatrix}. \quad (16)$$

Conversely, and denoting the map components of the inverse $T^{-1} : \mathbb{R}^m \rightarrow \mathbb{R}^m$ of T by $S_i \equiv (T^{-1})_i$, $i = 1, \dots, m$, one has that the i -th map component S_i only depends on the values $\{y_j\}_{j=1}^i$ of the first i random variables $\{\mathcal{Y}_j\}_{j=1}^i$:

$$S(y) = \begin{bmatrix} S_1(y_1) \\ S_2(y_1, y_2) \\ \vdots \\ S_m(y_1, y_2, \dots, y_m) \end{bmatrix} \equiv T^{-1}(y). \quad (17)$$

To ensure positivity of the densities (refer to equations (3) and (4) of the main text), each map component T_i in equation (16) must be differentiable with respect to x_i , and we must have that $\partial_{x_i} T_i > 0$, for every $i = 1, \dots, m$. Similarly, each component S_i in equation (17) of the inverse map T^{-1} of T must satisfy said properties with respect to the variables y_i [4, 24].

We now briefly describe the method of constructing and computing (the components of) the triangular transport map as it has been implemented in [2]. Let $\gamma(dy) = \frac{1}{\sqrt{2\pi}}e^{-y^2/2}dy$ be the standard Gaussian measure on \mathbb{R} . Consider the space $\mathbb{R}^{\mathbb{N}}$ (sometimes denoted \mathbb{R}^{∞}), where $\mathbb{N} = \{1, 2, \dots\}$ is the set of natural numbers, and the set $\mathbb{Z}_+^{\mathbb{N}}$, where $\mathbb{Z}_+ = \{0, 1, 2, \dots\}$ is the set of non-negative integers. For $y = (y_1, y_2, \dots) \in \mathbb{R}^{\mathbb{N}}$, the canonical projections $P^{(i)} : \mathbb{R}^{\mathbb{N}} \rightarrow \mathbb{R}^i$ are defined as $P^{(i)}(y) = (y_1, y_2, \dots, y_i)$. Similarly, if $\alpha = (\alpha_1, \alpha_2, \dots) \in \mathbb{Z}_+^{\mathbb{N}}$, and using the same notation for the canonical projection $P^{(i)} : \mathbb{Z}_+^{\mathbb{N}} \rightarrow \mathbb{Z}_+^i$, we have $P^{(i)}(\alpha) = (\alpha_1, \alpha_2, \dots, \alpha_i) \equiv \alpha^{(i)}$. Let $\gamma^{\mathbb{N}} = \gamma \times \gamma \times \dots$ be the infinite product Gaussian measure defined on the Borel σ -algebra $\mathcal{B}(\mathbb{R}^{\mathbb{N}})$. Then we obtain $P_{\#}^{(i)}(\gamma^{\mathbb{N}}) = \gamma^i = \underbrace{\gamma \times \gamma \times \dots \times \gamma}_{i \text{ times}}$ to be the i -variate Gaussian product measure on the Borel σ -algebra $\mathcal{B}(\mathbb{R}^i)$. Let $L^2(\mathbb{R}^i, \gamma^i)$ be the space of square integrable real valued functions on \mathbb{R}^i with respect to γ^i . For all $i \in \mathbb{N}$ consider the Sobolev spaces

$$H^1(\mathbb{R}^i, \gamma^i) = \left\{ f \in L^2(\mathbb{R}^i, \gamma^i) \mid \forall s : 1 \leq s \leq i, \frac{\partial f}{\partial y_s} \in L^2(\mathbb{R}^i, \gamma^i) \right\} \quad (18)$$

with norm, for every $f \in H^1(\mathbb{R}^i, \gamma^i)$, defined by

$$\|f\|_{H^1(\mathbb{R}^i, \gamma^i)} = \left[\|f\|_{L^2(\mathbb{R}^i, \gamma^i)}^2 + \sum_{s=1}^i \left\| \frac{\partial f}{\partial y_s} \right\|_{L^2(\mathbb{R}^i, \gamma^i)}^2 \right]^{\frac{1}{2}}, \quad (19)$$

and the spaces

$$V_i(\mathbb{R}^i, \gamma^i) = \left\{ f \in L^2(\mathbb{R}^i, \gamma^i) \mid \frac{\partial f}{\partial y_i} \in L^2(\mathbb{R}^i, \gamma^i) \right\}, \quad (20)$$

with norm

$$\|f\|_{V_i(\mathbb{R}^i, \gamma^i)} = \left[\|f\|_{L^2(\mathbb{R}^i, \gamma^i)}^2 + \left\| \frac{\partial f}{\partial y_i} \right\|_{L^2(\mathbb{R}^i, \gamma^i)}^2 \right]^{\frac{1}{2}}. \quad (21)$$

Clearly we have $H^1(\mathbb{R}^i, \gamma^i) \subset V_i(\mathbb{R}^i, \gamma^i) \subset L^2(\mathbb{R}^i, \gamma^i)$ for $i > 1$ and $H^1(\mathbb{R}, \gamma) = V_1(\mathbb{R}, \gamma)$. For $i > 1$ the space $V_i(\mathbb{R}^i, \gamma^i)$ can be constructed as a tensor product $L^2(\mathbb{R}^{i-1}, \gamma^{i-1}) \otimes H^1(\mathbb{R}, \gamma)$ equipped with the Hilbert-Schmidt norm, that is, if $f = g \otimes h$, where $g \in L^2(\mathbb{R}^{i-1}, \gamma^{i-1})$ and $h \in H^1(\mathbb{R}, \gamma)$, then $\|f\|_{V_i(\mathbb{R}^i, \gamma^i)} = \|g \otimes h\|_{HS} = \|g\|_{L^2(\mathbb{R}^{i-1}, \gamma^{i-1})} \|h\|_{H^1(\mathbb{R}, \gamma)}$.

Now, if $n \in \mathbb{Z}_+$, let h_n be the n -th Hermite polynomial on \mathbb{R} :

$$h_n(y) = \frac{(-1)^n}{\sqrt{n!}} e^{y^2/2} \frac{d^n}{dy^n} \left(e^{-y^2/2} \right). \quad (22)$$

Then the set $\{h_n\}_{n \geq 0}$ forms an orthonormal basis on the Hilbert space $L^2(\mathbb{R}, \gamma)$. Moreover, $\{h_n\}_{n \geq 0}$ forms an orthogonal basis on the Hilbert space $H^1(\mathbb{R}, \gamma)$ as well, with its inner product

$$\langle f, g \rangle_{H^1(\mathbb{R}, \gamma)} = \langle f, g \rangle_{L^2(\mathbb{R}, \gamma)} + \langle f', g' \rangle_{L^2(\mathbb{R}, \gamma)}, \quad (23)$$

for every $f, g \in H^1(\mathbb{R}, \gamma)$. More generally, the space of polynomials is dense in $L^2(\mathbb{R}, \gamma)$ and this implies that the space of polynomials on \mathbb{R}^i is dense in $L^2(\mathbb{R}^i, \gamma^i)$, for every $i \in \mathbb{N}$. Therefore, with the remark above in mind, we take as an orthonormal basis for the Hilbert space $V_i(\mathbb{R}^i, \gamma^i) \subset L^2(\mathbb{R}^i, \gamma^i)$ the set of polynomials

$$\left\{ \tilde{\mathcal{H}}_{\alpha^{(i)}}(y) = h_{\alpha_1}(y_1) h_{\alpha_2}(y_2) \cdots h_{\alpha_{i-1}}(y_{i-1}) \tilde{h}_{\alpha_i}(y_i) \mid \alpha^{(i)} \in \mathbb{Z}_+^i, y \in \mathbb{R}^i \right\}, \quad (24)$$

where the polynomials $\prod_{s=1}^{i-1} h_{\alpha_s}(y_s)$, $(\alpha_1, \alpha_2, \dots, \alpha_{i-1}) \in \mathbb{Z}_+^{i-1}$, form an orthonormal basis of $L^2(\mathbb{R}^{i-1}, \gamma^{i-1})$ and $\tilde{h}_{\alpha_i}(y_i) = h_{\alpha_i}(y_i)/\sqrt{\alpha_i + 1}$, $\alpha_i \in \mathbb{Z}_+$, form an orthonormal basis of $H^1(\mathbb{R}, \gamma)$ (the latter normalization follows from the property $h'_{n+1} = \sqrt{n+1} h_n$ of Hermite polynomials). Finally, let us consider the space

$$H^\infty(\mathbb{R}, \gamma) = \left\{ f \in L^2(\mathbb{R}, \gamma) \mid \forall s : s \in \mathbb{N}, f^{(s)} \in L^2(\mathbb{R}, \gamma) \right\} \quad (25)$$

of infinitely differentiable functions on \mathbb{R} . Using the definition (22) and integration by parts one can easily show that $\langle f, h_n \rangle_{L^2(\mathbb{R}, \gamma)} = 1/\sqrt{n!} \langle f^{(n)}, 1 \rangle_{L^2(\mathbb{R}, \gamma)}$ and therefore every function $f \in H^\infty(\mathbb{R}, \gamma)$ can be represented as

$$f(y) = \sum_{n=0}^{\infty} \frac{1}{\sqrt{n!}} \left\langle f^{(n)}, 1 \right\rangle_{L^2(\mathbb{R}, \gamma)} h_n(y). \quad (26)$$

This result has a straightforward generalization in arbitrary dimension $i \geq 1$. Namely, every infinitely differentiable function $f \in H^\infty(\mathbb{R}^i, \gamma^i)$, where

$$H^\infty(\mathbb{R}^i, \gamma^i) = \left\{ f \in L^2(\mathbb{R}^i, \gamma^i) \mid \alpha^{(i)} \in \mathbb{Z}_+^i \setminus \{\mathbf{0}\}, \frac{\partial^{|\alpha^{(i)}|} f}{\partial y^{\alpha_1} \dots \partial y^{\alpha_i}} \in L^2(\mathbb{R}^i, \gamma^i) \right\}, \quad (27)$$

can be represented as

$$f(y) = \sum_{|\alpha^{(i)}|=0}^{\infty} \frac{1}{\sqrt{\alpha^{(i)}!}} \left\langle \frac{\partial^{|\alpha^{(i)}|} f}{\partial y^{\alpha_1} \dots \partial y^{\alpha_i}}, 1 \right\rangle_{L^2(\mathbb{R}^i, \gamma^i)} \mathcal{H}_{\alpha^{(i)}}(y), \quad (28)$$

where $|\alpha^{(i)}| = \alpha_1 + \dots + \alpha_i$, $\alpha^{(i)}! = \alpha_1! \dots \alpha_i!$, and the polynomials $\mathcal{H}_{\alpha^{(i)}}(y) = h_{\alpha_1}(y_1) \dots h_{\alpha_i}(y_i)$, $\alpha^{(i)} \in \mathbb{Z}_+^i$, form an orthonormal basis for $L^2(\mathbb{R}^i, \gamma^i)$.

The map components $\{S_i\}_{i=1}^m$ in equation (17) are sought via *rectification operators* $\{\mathcal{R}_i\}_{i=1}^m$ of the form

$$\mathcal{R}_i(f_i)(y_1, \dots, y_i) = f_i(y_1, \dots, y_{i-1}, 0) + \int_0^{y_i} g(\partial_t f_i(y_1, \dots, y_{i-1}, t)) dt, \quad (29)$$

that take sufficiently smooth non-monotone functions $f_i : \mathbb{R}^i \rightarrow \mathbb{R}$, $i = 1, \dots, m$, and transform them into monotone increasing functions S_i of their last argument y_i (see (17)). In equation (29) the function $g : \mathbb{R} \rightarrow \mathbb{R}^+$ is bijective and positive-valued. As discussed in [2], the choice of the function g in equation (29) has significant impact on the properties of the optimization problem (14) (refer to Section 4.1 of the main text) solved in order to compute, or learn, the transport map. The soft-plus function $g(z) = \log(1 + \exp(z))$, whose inverse is $g^{-1}(z) = \log(\exp(z) - 1)$, is one appropriate choice.

For each $i = 1, \dots, m$, the function f_i in equation (29) is represented as an M_i -term linear combination of basis functions from the set (24) (a finite M_i -dimensional approximation)

$$f_i(y_1, \dots, y_i) = \sum_{\alpha^{(i)} \in \Lambda^{(i)}} c_{\alpha^{(i)}} \tilde{\mathcal{H}}_{\alpha^{(i)}}(y_1, \dots, y_i), \quad (30)$$

where, for each $i = 1, \dots, m$:

- $\Lambda^{(i)} \subset \mathbb{Z}_+^i$ is a *finite* set of multi-indices $(\alpha_1^{(s)}, \alpha_2^{(s)}, \dots, \alpha_i^{(s)})_{s=1}^{M_i}$, where $M_i = \text{Card}(\Lambda^{(i)})$,
- $c_{\alpha^{(i)}} \in \mathbb{R}$ are real-valued coefficients (coordinates with respect to the basis), and

- $\tilde{\mathcal{H}}_{\alpha^{(i)}} : \mathbb{R}^i \rightarrow \mathbb{R}$ are the basis functions of the Hilbert space $V_i(\mathbb{R}^i, \gamma^i)$ previously described (refer to (24)).

Let us now give an outline of the adaptive transport map algorithm applied in our computations. The sets (of active indices which identify the sets of active variables – refer to Figure 3 of the main text) $\Lambda^{(i)}$ in equation (30) are constructed by a greedy algorithm inspired by the work from [26]. Namely, starting with a set $\Lambda_0^{(i)} = \emptyset$ one constructs a sequence $\{\Lambda_t^{(i)}\}_{t \geq 0}$ of *downward closed* sets. A set $\Lambda_t^{(i)} \subset \mathbb{Z}_+^i$ is downward closed if $\alpha^{(i)} \in \Lambda_t^{(i)}$ and $\alpha'^{(i)} \leq \alpha^{(i)} \implies \alpha'^{(i)} \in \Lambda_t^{(i)}$, where $\alpha'^{(i)} \leq \alpha^{(i)}$ means $\alpha'_s \leq \alpha_s$, for $1 \leq s \leq i$. The *reduced margin* $\mathcal{RM}(\Lambda_t^{(i)})$ of $\Lambda_t^{(i)}$ is defined as

$$\mathcal{RM}(\Lambda_t^{(i)}) = \left\{ \alpha^{(i)} \notin \Lambda_t^{(i)} \mid \alpha^{(i)} - \epsilon_{(s)}^{(i)} \in \Lambda_t^{(i)}, \forall s : 1 \leq s \leq i, \alpha_s \neq 0 \right\}, \quad (31)$$

where the multi-index $\epsilon_{(s)}^{(i)} = (0, \dots, 1_s, \dots, 0) \in \mathbb{Z}_+^i$ has the only non-zero entry equal to 1 at position s . If $\Lambda_t^{(i)}$ is downward closed, then $\Lambda_t^{(i)} \cup \{\alpha_t^{(i)}\}$ is downward closed for any $\alpha_t^{(i)} \in \mathcal{RM}(\Lambda_t^{(i)})$. Then every consecutive iteration $\Lambda_{t+1}^{(i)} = \Lambda_t^{(i)} \cup \{\alpha_t^{*(i)}\}$ is constructed with $\alpha_t^{*(i)} \notin \Lambda_t^{(i)}$ and $\alpha_t^{*(i)} \in \mathcal{RM}(\Lambda_t^{(i)})$ such that it achieves the *best* next step approximation f_i^{t+1} to f_i in (30).

Cross-validation [14] is employed to determine the maximal cardinality M_i^{\max} of $\Lambda_t^{(i)}$ (that is, the step $t = M_i^{\max}$ at which to stop adaptation), without overfitting the data. This results in an optimal value $M_i = \text{Card}(\Lambda^{(i)}) \leq M_i^{\max}$ and an approximation f_i which is thus *adapted* to the size of the training sample. The full details are provided in [2]. The greedy, incremental search for values $M_i = \text{Card}(\Lambda^{(i)}) \leq M_i^{\max}$ of the cardinalities of the sets $\Lambda^{(i)}$ leads to numerical efficiency in the algorithm (as the number of unknowns to determine in equation (30) grows quickly with increasing i and $\text{Card}(\Lambda^{(i)})$), as well as numerical stability, particularly when the amount of training data is “small”.

B Appendix: Supplementary Material for Computational Experiments with Adaptive Transport Maps

For the computational experiments reported in this Appendix and in Section 5.2.2 of the main text, which employ adaptive transport maps [2, 3], we work with a subset of six genes from those present both in the GSE43151 data set available from [21] and pathway hsa04650 from the KEGG database [16]. This pathway also ranked as one of the top pathways showing significant differential activation in response to low-dose radiation, as compared to zero-dose, based on the pathway ranking procedure from [23]. We hence use it for selecting genes (associated with the random variables) for the present computational experiments. The selected subset of genes and additional information about them appear in Table 1 and Figure 14.

As indicated in Section 5.2.2 of the main text, in order to assess the robustness of the results obtained from Algorithm 2, “Gathering statistics from transport maps sparsity patterns”, with respect to ordering of the random variables, we carried out the computational experiments described in Section 5.2.2 and, in particular, summarized via Figures 10–11 of the main text, using 20 different permutations $\{\sigma_p(\mathcal{Y})\}_{p=1}^{20}$ of the ordered set $\mathcal{Y} \equiv (\mathcal{Y}_j)_{j=1}^6$ of random variables. Specifically, Algorithm 2 was executed for each of the 20 permutations $\{\sigma_p(\mathcal{Y})\}_{p=1}^{20}$ listed in Table 2. The results were then analyzed individually for each permutation, as well as collectively after mapping the results obtained for each of the 20 permutations $\{\sigma_p(\mathcal{Y})\}_{p=1}^{20}$ to the random variable ordering corresponding to the identity permutation $\sigma_1(\mathcal{Y})$. The outcome of this exercise is summarized next and in Figure 12 of the main text.

Gene ID	Official Symbol	Official Full Name
5530	PPP3CA	protein phosphatase 3 catalytic subunit alpha
5532	PPP3CB	protein phosphatase 3 catalytic subunit beta
5533	PPP3CC	protein phosphatase 3 catalytic subunit gamma
5534	PPP3R1	protein phosphatase 3 regulatory subunit B, alpha
4472	NFATC1	nuclear factor of activated T cells 1
4473	NFATC2	nuclear factor of activated T cells 2

Table 1: Gene IDs with the corresponding official symbol and full name. Source of information: <https://www.ncbi.nlm.nih.gov/gene>

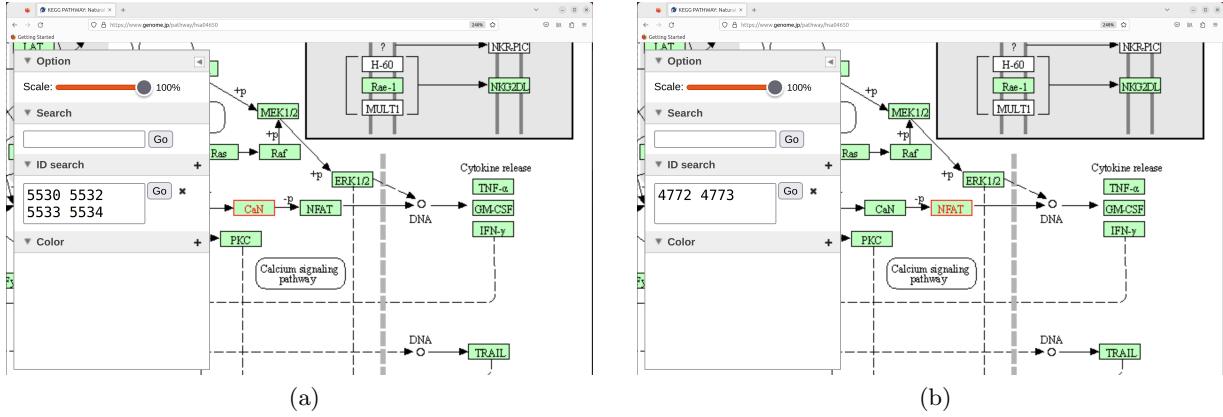


Figure 14: Segment of pathway hsa04650 containing genes 5530, 5532, 5533, 5534 (Subfigure 14a, CaN gene product, highlighted in red) and genes 4772, 4773 (Subfigure 14b, NFAT gene product, highlighted in red). Source of search tool and screenshots: <https://www.genome.jp/pathway/hsa04650>. KEGG pathway map notation: https://www.genome.jp/kegg/document/help_pathway.html

Firstly, persistence of patterns of high-valued frequency counts resulting from the computational experiments, as described in Figures 10–11 for the permutation $\sigma_1(\mathcal{Y})$ case, was also observed when executing Algorithm 2 for each of the 19 permutations $\{\sigma_m(\mathcal{Y})\}_{m=2}^{20}$. As one example illustrating this, we display in Figures 15–16, for the permutation $\sigma_{20}(\mathcal{Y})$ case, the analogues of Figures 10–11 from the main text. Note, however, that the patterns from Figure 10 versus the corresponding ones from Figure 15 (similarly, Figure 11 versus Figure 16) are different because each were computed for different permutations (namely, $\sigma_1(\mathcal{Y})$ and $\sigma_{20}(\mathcal{Y})$) of the random variables.

Now, to more easily compare and collect the results obtained for the 20 different permutations $\{\sigma_p(\mathcal{Y})\}_{p=1}^{20}$, we can map the statistics gathered for each of the permutations to the random variable ordering corresponding to the identity permutation $\sigma_1(\mathcal{Y}) = (\mathcal{Y}_j)_{j=1}^6$. Precisely, given the matrices $B_k^{(N, \sigma_p)}$ containing the frequency counts resulting from the transport maps sparsity patterns in a series of N transport maps computed for each class $k \in \{0, 1\}$ and, within each class, for the permutations $\{\sigma_p(\mathcal{Y})\}_{p=1}^{20}$ (see line 16 of Algorithm 2), we define new matrices:

1. $P_k^{(N, \sigma_p)} = \sigma_p^{-1} \left(B_k^{(N, \sigma_p)} \right)$: Lower triangular matrix storing the frequency counts from the matrix $B_k^{(N, \sigma_p)}$, rearranged after mapping from the ordering of the random variables corresponding to the permutation $\sigma_p(\mathcal{Y})$ to that for the identity permutation $\sigma_1(\mathcal{Y}) = (\mathcal{Y}_j)_{j=1}^6$, that is $P_k^{(N, \sigma_p)}(j, i) = B_k^{(N, \sigma_p)}(\min(\sigma_p(j), \sigma_p(i)), \max(\sigma_p(j), \sigma_p(i)))$ (see lines 12–14 of Algorithm 3).

$\mathcal{Y} \equiv (\mathcal{Y}_j)_{j=1}^6$	Gene ID					
	5533	5534	5530	5532	4472	4473
$\sigma_1(\mathcal{Y})$	\mathcal{Y}_1	\mathcal{Y}_2	\mathcal{Y}_3	\mathcal{Y}_4	\mathcal{Y}_5	\mathcal{Y}_6
$\sigma_2(\mathcal{Y})$	\mathcal{Y}_4	\mathcal{Y}_3	\mathcal{Y}_2	\mathcal{Y}_1	\mathcal{Y}_5	\mathcal{Y}_6
$\sigma_3(\mathcal{Y})$	\mathcal{Y}_1	\mathcal{Y}_2	\mathcal{Y}_3	\mathcal{Y}_4	\mathcal{Y}_6	\mathcal{Y}_5
$\sigma_4(\mathcal{Y})$	\mathcal{Y}_4	\mathcal{Y}_3	\mathcal{Y}_2	\mathcal{Y}_1	\mathcal{Y}_6	\mathcal{Y}_5
$\sigma_5(\mathcal{Y})$	\mathcal{Y}_6	\mathcal{Y}_5	\mathcal{Y}_4	\mathcal{Y}_3	\mathcal{Y}_2	\mathcal{Y}_1
$\sigma_6(\mathcal{Y})$	\mathcal{Y}_5	\mathcal{Y}_6	\mathcal{Y}_1	\mathcal{Y}_2	\mathcal{Y}_3	\mathcal{Y}_4
$\sigma_7(\mathcal{Y})$	\mathcal{Y}_1	\mathcal{Y}_2	\mathcal{Y}_5	\mathcal{Y}_3	\mathcal{Y}_6	\mathcal{Y}_4
$\sigma_8(\mathcal{Y})$	\mathcal{Y}_6	\mathcal{Y}_5	\mathcal{Y}_3	\mathcal{Y}_4	\mathcal{Y}_1	\mathcal{Y}_2
$\sigma_9(\mathcal{Y})$	\mathcal{Y}_3	\mathcal{Y}_2	\mathcal{Y}_6	\mathcal{Y}_1	\mathcal{Y}_5	\mathcal{Y}_4
$\sigma_{10}(\mathcal{Y})$	\mathcal{Y}_3	\mathcal{Y}_1	\mathcal{Y}_2	\mathcal{Y}_5	\mathcal{Y}_6	\mathcal{Y}_4
$\sigma_{11}(\mathcal{Y})$	\mathcal{Y}_6	\mathcal{Y}_5	\mathcal{Y}_4	\mathcal{Y}_2	\mathcal{Y}_3	\mathcal{Y}_1
$\sigma_{12}(\mathcal{Y})$	\mathcal{Y}_6	\mathcal{Y}_4	\mathcal{Y}_2	\mathcal{Y}_1	\mathcal{Y}_3	\mathcal{Y}_5
$\sigma_{13}(\mathcal{Y})$	\mathcal{Y}_4	\mathcal{Y}_5	\mathcal{Y}_3	\mathcal{Y}_1	\mathcal{Y}_6	\mathcal{Y}_2
$\sigma_{14}(\mathcal{Y})$	\mathcal{Y}_5	\mathcal{Y}_2	\mathcal{Y}_1	\mathcal{Y}_6	\mathcal{Y}_4	\mathcal{Y}_3
$\sigma_{15}(\mathcal{Y})$	\mathcal{Y}_3	\mathcal{Y}_5	\mathcal{Y}_2	\mathcal{Y}_4	\mathcal{Y}_1	\mathcal{Y}_6
$\sigma_{16}(\mathcal{Y})$	\mathcal{Y}_4	\mathcal{Y}_3	\mathcal{Y}_1	\mathcal{Y}_6	\mathcal{Y}_5	\mathcal{Y}_2
$\sigma_{17}(\mathcal{Y})$	\mathcal{Y}_2	\mathcal{Y}_4	\mathcal{Y}_1	\mathcal{Y}_6	\mathcal{Y}_5	\mathcal{Y}_3
$\sigma_{18}(\mathcal{Y})$	\mathcal{Y}_6	\mathcal{Y}_4	\mathcal{Y}_2	\mathcal{Y}_5	\mathcal{Y}_3	\mathcal{Y}_1
$\sigma_{19}(\mathcal{Y})$	\mathcal{Y}_6	\mathcal{Y}_3	\mathcal{Y}_4	\mathcal{Y}_2	\mathcal{Y}_1	\mathcal{Y}_5
$\sigma_{20}(\mathcal{Y})$	\mathcal{Y}_4	\mathcal{Y}_2	\mathcal{Y}_5	\mathcal{Y}_6	\mathcal{Y}_1	\mathcal{Y}_3

Table 2: Different permutations $\{\sigma_p(\mathcal{Y})\}_{p=1}^{20}$ of the gene IDs from Table 1, used for the computational experiments reported in this Appendix and in Section 5.2.2 of the main text. For each $p = 1, 2, \dots, 20$, we have $\sigma_p(\mathcal{Y}) = (\mathcal{Y}_{\sigma_p^{-1}(j)})_{j=1}^6$. Note that σ_1 is the identity.

An entry $P_k^{(N, \sigma_p)}(j, i)$ in the lower triangular portion of the matrix $P_k^{(N, \sigma_p)}$ thus contains a frequency count reflecting a dependency “strength” between the random variables \mathcal{Y}_j and \mathcal{Y}_i , obtained after computing a series of N transport maps with an ordering $\sigma_p(\mathcal{Y})$ of the random variables, after being mapped back (i.e., rearranged) so that it can be compared with the matrix of frequency counts obtained from the computation of N transport maps with an ordering $\sigma_1(\mathcal{Y})$ of the random variables or another matrix of frequency counts corresponding to another random variable ordering $\sigma_q(\mathcal{Y})$ after an analogous “normalization” (via the matrices $P_k^{(N, \sigma_p)}$). Such “normalization” simplifies comparison of results between separate sets of runs for each one of the 20 different permutations $\{\sigma_p(\mathcal{Y})\}_{p=1}^{20}$. An example is provided in Figures 17–18 for the instance $N=200$ of runs for permutations $\sigma_1(\mathcal{Y})$ and $\sigma_{20}(\mathcal{Y})$, where one can observe (qualitatively) good agreement between the resulting patterns of high-valued frequency counts. We observed (qualitatively) the same patterns with each one of the remaining permutations of random variables in Table 2, after computing a series of $N=200$ transport maps and subsequent “normalization” (in the matrices $P_k^{(N, \sigma_p)}$ – see line 14 of Algorithm 3). This shows robustness of the numerical method and its *invariance* with respect to the action of elements of the group of permutations \mathcal{S}_6 when identifying the dependence structure of the set of random variables $\{\mathcal{Y}_j\}_{j=1}^6$ as inferred from the sparsity patterns of the computed transport maps or, equivalently, from the structure of the corresponding estimated target densities.

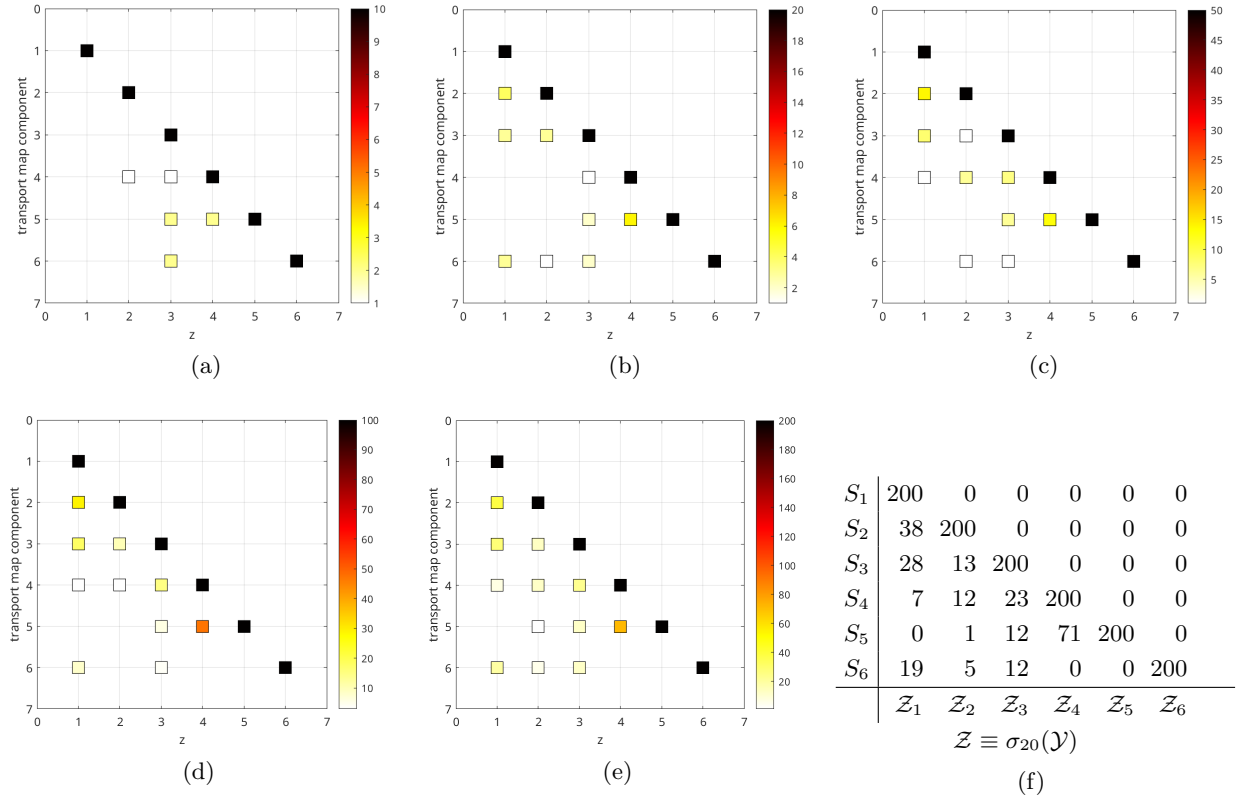


Figure 15: Aggregated sparsity patterns from adaptive transport map approximations to data distributions for different subsets of the zero-dose radiation data samples. The permutation on the ordered set $\mathcal{Y} \equiv (\mathcal{Y}_j)_{j=1}^6$ of random variables for the computational experiments summarized in Subfigures 15a–15f is that listed as permutation $\sigma_{20}(\mathcal{Y})$ in Table 2. As in Figure 10 of the main text, subsets of samples consisting of half the number of total samples (which for the zero-dose radiation class is 18) were generated from random permutations of the GSE43151 data set sample ordering. In Subfigures 15a, 15b, 15c, 15d, and 15e are represented the sparsity patterns corresponding to, respectively, 10, 20, 50, 100, and 200 such sample subsets. By aggregating results for increasing numbers of sample subsets, patterns of high-valued frequency counts are seen to emerge and persist. For reference, Subfigure 15f shows the values for the frequency counts corresponding to the sparsity pattern from Subfigure 15e. In other words, the matrix shown in Subfigure 15f is the matrix $B_0^{(200, \sigma_{20})}$ from Algorithm 2, lines 12–19, resulting from the execution of Algorithm 2 using permutation $\sigma_{20}(\mathcal{Y})$. To simplify notation in Subfigure 15f, we denote $S \equiv T^{-1}$ for the inverse T^{-1} of a transport map T .

2. $Q_k^{(\tilde{N})}$: Lower triangular matrix accumulating the frequency counts from the matrices $P_k^{(N, \sigma_p)}$ defined above. That is, for a given value of N runs and for each class $k \in \{0, 1\}$,

$$Q_k^{(\tilde{N})} = \sum_{p=1}^{n_{\text{perm}}} P_k^{(N, \sigma_p)}, \quad (32)$$

where $n_{\text{perm}}=20$ denotes the number of permutations and $\tilde{N} = N \times n_{\text{perm}}$. This summarizes frequency counts resulting from runs for all permutations $\{\sigma_p(\mathcal{Y})\}_{p=1}^{20}$, collectively, as illustrated in Figure 12 of the main text.

The above described matrices $P_k^{(N, \sigma_p)}$ and $Q_k^{(\tilde{N})}$ are created as outlined in Algorithm 3.

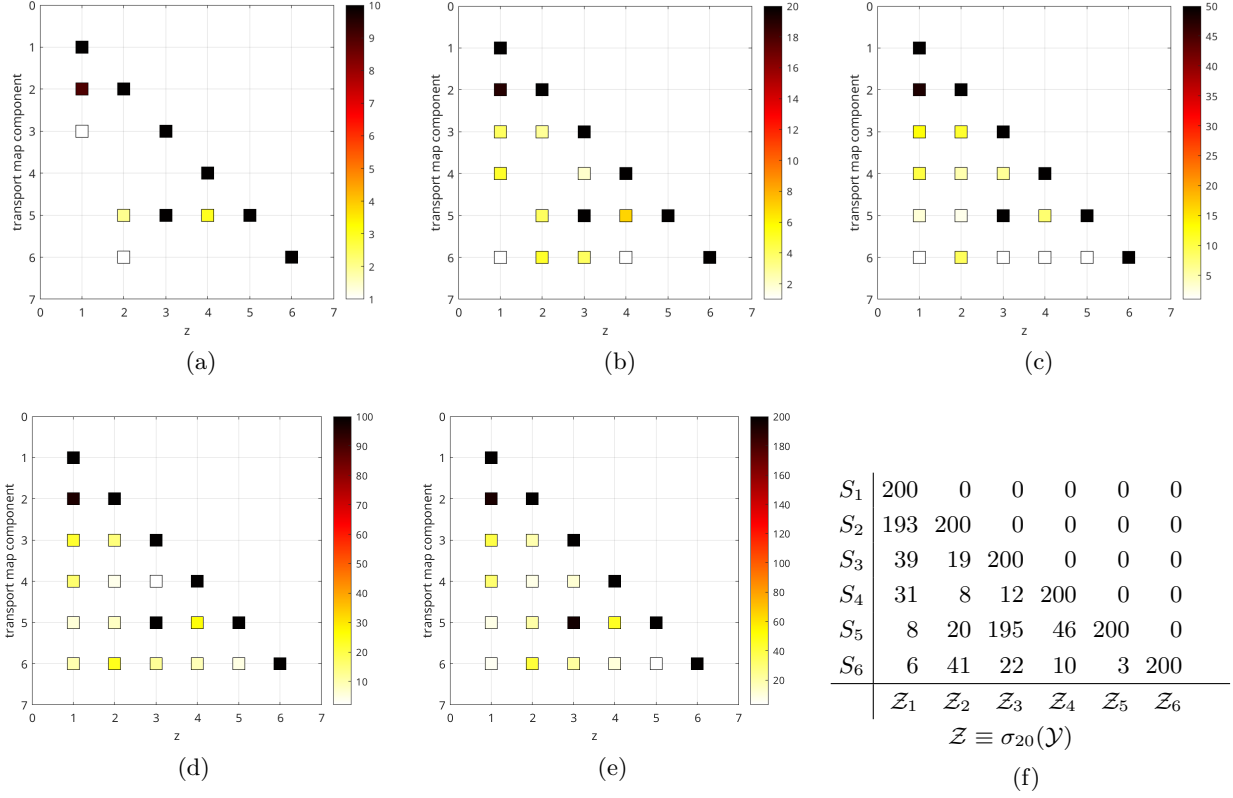
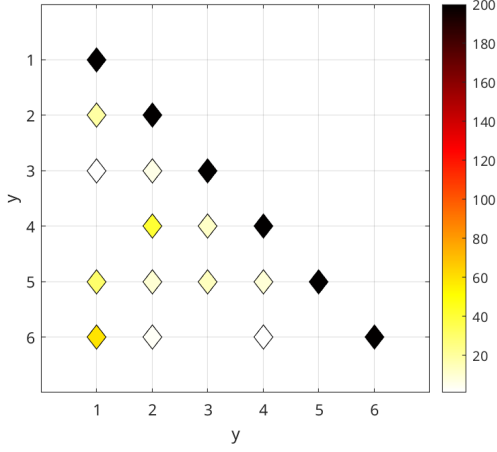


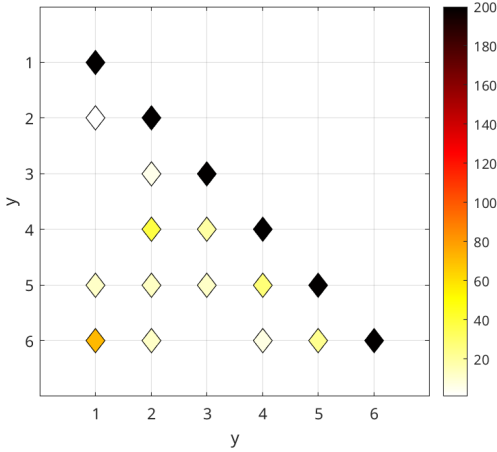
Figure 16: Aggregated sparsity patterns from adaptive transport map approximations to data distributions for different subsets of the low-dose radiation data samples. The permutation on the ordered set $\mathcal{Y} \equiv (\mathcal{Y}_j)_{j=1}^6$ of random variables for the computational experiments summarized in Subfigures 16a–16f is that listed as permutation $\sigma_{20}(\mathcal{Y})$ in Table 2. As in Figure 11 of the main text, subsets of samples consisting of half the number of total samples (which for the low-dose radiation class is 87) were generated from random permutations of the GSE43151 data set sample ordering. In Subfigures 16a, 16b, 16c, 16d, and 16e are represented sparsity patterns corresponding to, respectively, 10, 20, 50, 100, and 200 such sample subsets. As for the zero-dose radiation class in Figure 15, by aggregating results for increasing numbers of sample subsets, patterns of high-valued frequency counts are seen to emerge and persist. For reference, Subfigure 16f shows the values for the frequency counts corresponding to the sparsity pattern from Subfigure 16e. In other words, the matrix shown in Subfigure 16f is the matrix $B_1^{(200, \sigma_{20})}$ from Algorithm 2, lines 12–19, resulting from the execution of Algorithm 2 using permutation $\sigma_{20}(\mathcal{Y})$. To simplify notation in Subfigure 16f, we denote $S \equiv T^{-1}$ for the inverse T^{-1} of a transport map T .



(a) $P_0^{(200, \sigma_1)}$

\mathcal{Y}_1	200	0	0	0	0	0
\mathcal{Y}_2	19	200	0	0	0	0
\mathcal{Y}_3	1	6	200	0	0	0
\mathcal{Y}_4	0	41	12	200	0	0
\mathcal{Y}_5	30	10	14	9	200	0
\mathcal{Y}_6	59	3	0	1	0	200

(b) $P_0^{(200, \sigma_1)}$

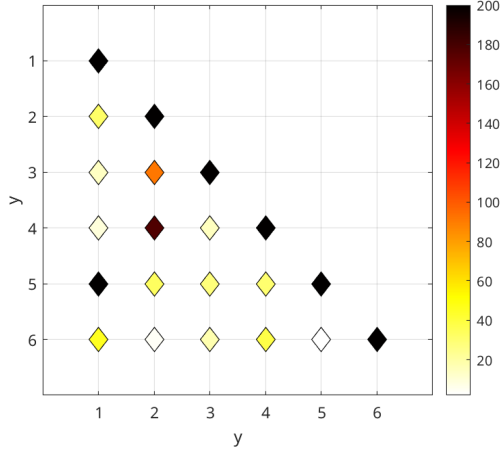


(c) $P_0^{(200, \sigma_{20})}$

\mathcal{Y}_1	200	0	0	0	0	0
\mathcal{Y}_2	1	200	0	0	0	0
\mathcal{Y}_3	0	5	200	0	0	0
\mathcal{Y}_4	0	38	19	200	0	0
\mathcal{Y}_5	12	13	12	28	200	0
\mathcal{Y}_6	71	12	0	7	23	200

(d) $P_0^{(200, \sigma_{20})}$

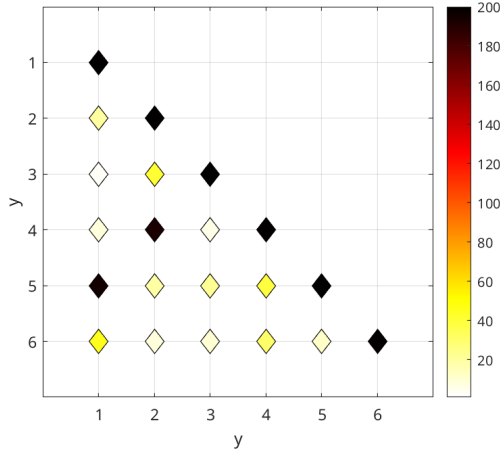
Figure 17: Aggregated sparsity patterns and associated frequency counts from adaptive transport map approximations to data distributions for different subsets of the zero-dose radiation data samples. The assignment of genes to the ordered set $\mathcal{Y} \equiv (\mathcal{Y}_j)_{j=1}^6$ of random variables for the computational experiments summarized in Subfigures 17a–17b is that listed as permutation $\sigma_1(\mathcal{Y})$ in Table 2, whereas for Subfigures 17c–17d it is that listed as permutation $\sigma_{20}(\mathcal{Y})$. To facilitate comparison, the frequency counts shown above were mapped to the random variable ordering corresponding to the identity permutation $\sigma_1(\mathcal{Y})$, as described in Algorithm 3. Specifically, the matrices shown in Subfigures 17b and 17d resulted from line 14 of Algorithm 3. Good qualitative agreement is observed between the high-valued frequency counts for $P_0^{(200, \sigma_1)}$ (Subfigure 17a) and those for $P_0^{(200, \sigma_{20})}$ (Subfigure 17c), in spite of quantitative differences (particularly for low-valued frequency counts).



(a) $P_1^{(200, \sigma_1)}$

\mathcal{Y}_1	200	0	0	0	0	0
\mathcal{Y}_2	32	200	0	0	0	0
\mathcal{Y}_3	14	91	200	0	0	0
\mathcal{Y}_4	9	177	15	200	0	0
\mathcal{Y}_5	200	33	28	30	200	0
\mathcal{Y}_6	46	4	18	38	2	200
	\mathcal{Y}_1	\mathcal{Y}_2	\mathcal{Y}_3	\mathcal{Y}_4	\mathcal{Y}_5	\mathcal{Y}_6

(b) $P_1^{(200, \sigma_1)}$



(c) $P_1^{(200, \sigma_{20})}$

\mathcal{Y}_1	200	0	0	0	0	0
\mathcal{Y}_2	20	200	0	0	0	0
\mathcal{Y}_3	3	41	200	0	0	0
\mathcal{Y}_4	8	193	6	200	0	0
\mathcal{Y}_5	195	19	22	39	200	0
\mathcal{Y}_6	46	8	10	31	12	200
	\mathcal{Y}_1	\mathcal{Y}_2	\mathcal{Y}_3	\mathcal{Y}_4	\mathcal{Y}_5	\mathcal{Y}_6

(d) $P_1^{(200, \sigma_{20})}$

Figure 18: Aggregated sparsity patterns and associated frequency counts from adaptive transport map approximations to data distributions for different subsets of the low-dose radiation data samples. The assignment of genes to the ordered set $\mathcal{Y} \equiv (\mathcal{Y}_j)_{j=1}^6$ of random variables for the computational experiments summarized in Subfigures 18a–18b is that listed as permutation $\sigma_1(\mathcal{Y})$ in Table 2, whereas for Subfigures 18c–18d it is that listed as permutation $\sigma_{20}(\mathcal{Y})$. To facilitate comparison, the frequency counts shown above were mapped to the random variable ordering corresponding to the identity permutation $\sigma_1(\mathcal{Y})$, as described in Algorithm 3. Specifically, the matrices shown in Subfigures 18b and 18d resulted from line 14 of Algorithm 3. Good qualitative agreement is observed between the high-valued frequency counts for $P_1^{(200, \sigma_1)}$ (Subfigure 18a) and those for $P_1^{(200, \sigma_{20})}$ (Subfigure 18c), in spite of quantitative differences (particularly for low-valued frequency counts).

Algorithm 3

```
1: Let  $m(= 6)$  denote the number of random variables
2: Let  $n_{\text{perm}}(= 20)$  denote the number of permutations  $\sigma_p(\mathcal{Y})$  of the random variables
3: Let  $N$  denote a given number of runs
4: Let  $\tilde{N} = N \times n_{\text{perm}}$ 
5: Let  $K(= 2)$  denote the number of classes
6: for  $k = 0$  to  $K - 1$  do
7:   Initialize  $Q_k^{(\tilde{N})}$  to the  $m \times m$  zero matrix
8:   for  $p = 1$  to  $n_{\text{perm}}$  do
9:     Initialize  $P_k^{(N, \sigma_p)}$  to the  $m \times m$  zero matrix
10:    for  $j = 1$  to  $m$  do
11:      for  $i = 1$  to  $j$  do
12:         $\tilde{j} = \min(\sigma_p(j), \sigma_p(i))$ 
13:         $\tilde{i} = \max(\sigma_p(j), \sigma_p(i))$ 
14:         $P_k^{(N, \sigma_p)}(j, i) = B_k^{(N, \sigma_p)}(\tilde{j}, \tilde{i})$  ▷ frequency count reflecting dependency
15:        “strength” between random variables
16:         $\mathcal{Y}_j$  and  $\mathcal{Y}_i$ , of  $N$  runs for permutation
17:         $\sigma_p(\mathcal{Y})$ 
18:         $Q_k^{(\tilde{N})}(j, i) = Q_k^{(\tilde{N})}(j, i) + P_k^{(N, \sigma_p)}(j, i)$  ▷ accumulate frequency counts
19:        from line 14
20:      end for
21:    end for
22:  end for
23: end for
```

References

- [1] J. P. Agnelli, M. Cadeiras, E. G. Tabak, C. V. Turner, and E. Vanden-Eijnden. Clustering and classification through normalizing flows in feature space. *Multiscale Model. Simul.*, 8(5):1784–1802, 2010.
- [2] R. Baptista, Y. Marzouk, and O. Zahm. On the representation and learning of monotone triangular transport maps, 2022.
- [3] R. Baptista and P.-B. Rubio. AdaptiveTransportMaps software library, 2022. <https://github.com/baptistar/ATM>.
- [4] V. I. Bogachev, A. V. Kolesnikov, and K. V. Medvedev. Triangular transformations of measures. *Sbornik: Mathematics*, 196(3), 2005.
- [5] S. Boluki, M. S. Esfahani, X. Qian, and E. A. Dougherty. Incorporating biological prior knowledge for Bayesian learning via maximal knowledge-driven information priors. *BMC Bioinformatics*, 18, 2017.
- [6] K. Cao, Q. Gong, Y. Hong, and L. Wan. A unified computational framework for single-cell data integration with optimal transport. *Nat. Commun.*, 13(1), 2022.
- [7] L. de Torrenté, S. Zimmerman, M. Suzuki, M. Christopeit, J. M. Greally, and J. C. Mar. The shape of gene expression distributions matter: how incorporating distribution shape improves the interpretation of cancer transcriptomic data. *BMC Bioinformatics*, 21, 2020.
- [8] L. Dinh, J. Sohl-Dickstein, and S. Bengio. Density estimation using Real NVP. 2017.
- [9] R. Edgar, M. Domrachev, and A. E. Lash. Gene Expression Omnibus: NCBI gene expression and hybridization array data repository. *Nucleic Acids Res.*, 30(1):207–210, 2002.
- [10] T. A. El Moselhy and Y. M. Marzouk. Bayesian inference with optimal maps. *J. Comput. Phys.*, 231(23):7815–7850, 2012.
- [11] M. Gabrié, G. M. Rotskoff, and E. Vanden-Eijnden. Adaptive Monte Carlo augmented with normalizing flows. *Proc. Natl. Acad. Sci.*, 119(10), 2022.
- [12] F. Ghanegolmohammadi, S. Ohnuki, and Y. Ohya. Assignment of unimodal probability distribution models for quantitative morphological phenotyping. *BMC Biol*, 20, 2022.
- [13] F. Gossi, P. Pati, P. Chouvardas, A. L. Martinelli, M. Kruithof-de Julio, and M. A. Rapsomaniki. Matching Single Cells Across Modalities with Contrastive Learning and Optimal Transport. *Brief. Bioinform.*, 24(3), 2023.
- [14] T. Hastie, R. Tibshirani, and J.H. Friedman. *The Elements of Statistical Learning: Data Mining, Inference, and Prediction*. Springer Series in Statistics. Springer, Switzerland, 2009.
- [15] P. R. Johnstone. Github repository, 2023. https://github.com/1austrartsua1/KEGG_ML.
- [16] M. Kanehisa and S. Goto. KEGG: Kyoto Encyclopedia of Genes and Genomes. *Nucleic Acids Res.*, 28(1):27–30, 2000.
- [17] M. Katzfuss and F. Schäfer. Scalable Bayesian transport maps for high-dimensional non-Gaussian spatial fields, 2023.

- [18] Markelle Kelly, Rachel Longjohn, and Kolby Nottingham. The UCI Machine Learning Repository, 1987–present. <https://archive.ics.uci.edu>.
- [19] A. V. Kolesnikov. Convexity inequalities and optimal transport of infinite-dimensional measures. *J. Math. Pures Appl.*, 83:1373–1404, 2004.
- [20] V. Lohweg. Banknote Authentication. UCI Machine Learning Repository, 2013.
- [21] X. Luo. Github repository, 2022. <https://github.com/Xihaier/Pathway-Analysis-of-Low-Dose-Radiation-Data>.
- [22] X. Luo, S. McCorkle, G. Park, V. López-Marrero, S. Yoo, E. R. Dougherty, X. Qian, F. J. Alexander, and B.-J. Yoon. Comprehensive analysis of gene expression profiles to radiation exposure reveals molecular signatures of low-dose radiation response. In *2022 IEEE International Conference on Bioinformatics and Biomedicine (BIBM)*, pages 2366–2374, 2022.
- [23] X. Luo, S. Niyakan, P. Johnstone, S. McCorkle, G. Park, V. López-Marrero, S. Yoo, E. R. Dougherty, X. Qian, F. J. Alexander, S. Jha, and B.-J. Yoon. Pathway-based analyses of gene expression profiles at low doses of ionizing radiation, 2023. *Submitted*.
- [24] Y. Marzouk, T. Moselhy, M. Parno, and A. Spantini. Sampling via measure transport: An introduction. In R. Ghanem, D. Higdon, and H. Owhadi, editors, *Handbook of Uncertainty Quantification*, pages 1–41. Springer International Publishing, Cham, 2016.
- [25] MathWorks. Statistics and machine learning toolbox, 2022. <https://www.mathworks.com/products/statistics.html>.
- [26] Giovanni Migliorati. Adaptive approximation by optimal weighted least-squares methods. *SIAM Journal on Numerical Analysis*, 57(5):2217–2245, 2019.
- [27] MIT Uncertainty Quantification Group. Software libraries, 2013–present. <https://uqgroup.mit.edu/software>.
- [28] MIT Uncertainty Quantification Group. TransportMaps software library, 2015–present. <https://transportmaps.mit.edu/docs/>.
- [29] R. E. Morrison, R. Baptista, and Y. Marzouk. Beyond normality: Learning sparse probabilistic graphical models in the non-Gaussian setting. In *Proceedings of the 31st International Conference on Neural Information Processing Systems, NIPS’17*, pages 2356–2366, Red Hook, NY, USA, 2017. Curran Associates Inc.
- [30] I. Nosel, A. Vaurijoux, J.-F. Barquinero, and G. Gruel. Characterization of gene expression profiles at low and very low doses of ionizing radiation. *DNA Repair*, 12(7):508–517, 2013.
- [31] F. Otto and C. Villani. Generalization of an inequality by Talagrand, and links with the logarithmic Sobolev inequality. *J. Funct. Anal.*, 173(2):361–400, 2000.
- [32] G. Papamakarios, E. Nalisnick, D. Jimenez Rezende, S. Mohamed, and B. Lakshminarayanan. Normalizing flows for probabilistic modeling and inference. *J. Mach. Learn. Res.*, 22(1), 2021.
- [33] G. Park, B.-J. Yoon, X. Luo, V. López-Marrero, P. Johnstone, S. Yoo, and F. Alexander. Automated extraction of molecular interactions and pathway knowledge using large language model, Galactica: Opportunities and challenges. In *The 22nd Workshop on Biomedical Natural Language Processing and BioNLP Shared Tasks*, pages 255–264, 2023.

- [34] G. Park, B.-J. Yoon, X. Luo, V. López-Marrero, P. Johnstone, S. Yoo, and F. J. Alexander. Comparative performance evaluation of large language models for extracting molecular interactions and pathway knowledge. 2023.
- [35] F. Pedregosa, G. Varoquaux, A. Gramfort, V. Michel, B. Thirion, O. Grisel, M. Blondel, P. Prettenhofer, R. Weiss, V. Dubourg, J. Vanderplas, A. Passos, D. Cournapeau, M. Brucher, M. Perrot, and E. Duchesnay. Scikit-learn: Machine learning in Python. *J. Mach. Learn. Res.*, 12:2825–2830, 2011. https://scikit-learn.org/stable/modules/generated/sklearn.metrics.f1_score.html.
- [36] G. Peyré and M. Cuturi. Computational optimal transport: With applications to data science. *Foundations and Trends[®] in Machine Learning*, 11(5–6):355–607, 2019.
- [37] F. Santambrogio. *Optimal Transport for Applied Mathematicians: Calculus of Variations, PDEs, and Modeling*. Progress in Nonlinear Differential Equations and Their Applications. Birkhäuser, Cham, 2015.
- [38] B.W. Silverman. *Density Estimation for Statistics and Data Analysis*. Monographs on Statistics and Applied Probability. Chapman & Hall, London, 1998.
- [39] A. Spantini, R. Baptista, and Y. Marzouk. Coupling techniques for nonlinear ensemble filtering. *SIAM Rev.*, 64(4):921–953, 2022.
- [40] A. Spantini, D. Bigoni, and Y. Marzouk. Inference via low-dimensional couplings. *J. Mach. Learn. Res.*, 19(1), 2018.
- [41] E. G. Tabak and C. V. Turner. A family of nonparametric density estimation algorithms. *Commun. Pure Appl. Math.*, 66(2):145–164, 2013.
- [42] E. G. Tabak and E. Vanden-Eijnden. Density estimation by dual ascent of the log-likelihood. *Commun. Math. Sci.*, 8(1):217–233, 2010.
- [43] C. Uhler and G. V. Shivashankar. Machine learning approaches to single-cell data integration and translation. *Proceedings of the IEEE*, 110(5):557–576, 2022.
- [44] C. Villani. *Optimal Transport: Old and New*. Springer Berlin, Heidelberg, 2009.
- [45] H. Yang and E. G. Tabak. Conditional density estimation, latent variable discovery, and optimal transport. *Commun. Pure Appl. Math.*, 75(3):610–663, 2022.